J. Fluid Mech. (2025), *vol.* 1019, A60, doi:10.1017/jfm.2025.10645

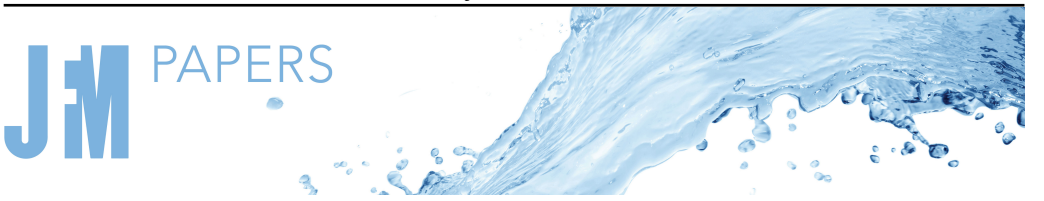

Correlations between streamwise velocity and temperature fluctuations in compressible turbulent channel flows from the perspective of coherent structures

Ruixin Li[1,2], **Lin Fu**[2,3] and **Chun-Xiao Xu**[1]

[1]Key Laboratory of Applied Mechanics, Ministry of Education, Institute of Fluid Mechanics, Department of Engineering Mechanics, Tsinghua University, Beijing 100084, PR China

[2]Department of Mechanical and Aerospace Engineering, The Hong Kong University of Science and Technology, Clear Water Bay, Kowloon, Hong Kong

[3]Department of Mathematics, The Hong Kong University of Science and Technology, Clear Water Bay, Kowloon, Hong Kong

Corresponding authors: Lin Fu, linfu@ust.hk; Chun-Xiao Xu, xucx@tsinghua.edu.cn

(Received 25 March 2025; revised 16 July 2025; accepted 31 August 2025)

In this work, the correlations between streamwise velocity and temperature fluctuations are investigated in compressible turbulent channel flows from the perspective of coherent structures. The intense fluctuation structures and quadrant-event structures of both velocity and temperature have been identified, extracted separately and compared. Analyses show that although their structure sizes are similar in the whole channel, high correlation only exists in the near-wall region with a high overlapping rate of the instantaneous structures. The hierarchy of the temperature structures are passively formed following the dynamic process of the velocity such as ejections, which contributes to the remaining correlation in the outer layer. However, this passive scalar property cannot provide the production mechanism in the outer layer according to the budget analysis after scale decomposition, and the interscale energy transfer progress is also different from the velocity fluctuation field. Therefore, the temperature structures deviate from the velocity structures in the outer layer and cannot be carried by the following dynamic process of the velocity such as sweeps, passively, which can be found from the conditional averaged structures. All of these findings provide a new perspective for understanding the velocity–temperature relationship in compressible channel flows.

Key words: boundary layer structure, turbulent boundary layers, turbulence theory

1. Introduction

In compressible wall-bounded flows, the relationship between streamwise velocity and temperature has attracted researchers' attention for a long time since there is a notable similarity between the momentum and energy transport (Fu *et al.* 2021; Cheng *et al.* 2024). Reynolds (1961) proposed the velocity–temperature relation for incompressible flows by inspecting the Reynolds-averaged equations and then the so-called Reynolds analogy becomes the joint name for the related research (Cheng *et al.* 2024). For the averaged field, the averaged streamwise velocity $\bar{u}$ and temperature $\bar{T}$ follow the quadratic relation

$$\frac{\bar{T}}{\bar{T}_\delta} = \frac{\bar{T}_w}{\bar{T}_\delta} + \frac{\bar{T}_* - \bar{T}_w}{\bar{T}_\delta}\frac{\bar{u}}{\bar{u}_\delta} + \frac{\bar{T}_\delta - \bar{T}_*}{\bar{T}_\delta}\left(\frac{\bar{u}}{\bar{u}_\delta}\right)^2, \tag{1.1}$$

where $\bar{T}_* = \bar{T}_\delta + \alpha\bar{u}_\delta^2/(2C_p)$. Here $\bar{u}_\delta$, $\bar{T}_\delta$ are the values at the edge of the boundary layer and $\bar{T}_w$ is the value on the wall. Here C_p is the constant-pressure specific heat capacity. The coefficient α has been set to 1 in the Crocco–Busemann relation, 0.9 in Walz's equation (Walz 1969) and generalized recovery factor in the generalized Reynolds analogy (Zhang *et al.* 2013). As for the fluctuation field, identifying the correlations between u' and T' (fluctuations of streamwise velocity and temperature corresponding to the Reynolds average) becomes much more challenging. Since Morkovin (1962) proposed the first set of relations called the strong Reynolds analogy (SRA), later, numerous modifications have been developed to improve the performance of SRA with different wall conditions (Huang, Coleman & Bradshaw 1995; Zhang *et al.* 2013). One kind of common form of SRA is written as (Cheng *et al.* 2024)

$$\frac{T'_{rms}}{(\gamma-1)\,Ma^2 u'_{rms}/\bar{u}} = \frac{1}{a\left(1-\partial\bar{T}_t/\partial\bar{T}\right)}, \tag{1.2}$$

where $\bar{T}_t$ is the averaged total temperature and Ma denotes the Mach number. The ratio of specific heats γ equals 1.4. The subscript '*rms*' denotes the root-mean-square of the variable. The coefficient a has been chosen as different values such as the turbulent Prandtl number Pr_t (Huang *et al.* 1995) or the reciprocal of the mixed Prandtl number $1/Pr_m$ (Brun *et al.* 2008).

Although the Reynolds analogy and SRA provide the equations that can describe the relation between streamwise velocity and temperature mathematically from the perspective of statistics, nothing about the flow itself can be comprehended. Cheng & Fu (2023) mentioned that the u'–T' coupling is strongest in the near-wall region and only remains notable in very large-scale motions (VLSMs) in the outer layer by employing the two-dimensional spectral linear stochastic estimation method. Cheng, Wei & Fu (2023) studied the quadrant events (Qs) for both momentum and heat flux in compressible channel flows and found that they both possess common features. These studies have provided some basic physical understanding. However, the physical mechanism behind these statistical phenomena is still unclear, i.e. the reason that u' and T' are highly correlated only in some specific regions needs to be figured out by further research. Thus, this work aims to fill this gap partially through the perspective of coherent structures.

Coherent structures have received intensive attention since they provide important insights into flow mechanisms and have the potential to guide turbulence modelling. Research on these structures starts from wall-bounded incompressible flows and mainly focuses on intense fluctuation structures (i.e. streaks) and Qs structures (Jeong *et al.* 1997; del Á lamo *et al.* 2006; Hutchins & Marusic 2007*a*; Mathis, Hutchins & Marusic

2009; Lozano-Durán *et al.* 2012; Lozano-Durán & Jiménez 2014; Baars, Hutchins & Marusic 2017; Hwang & Sung 2018*a*; Hwang, Lee & Sung 2020; Motoori & Goto 2021; Zhou, Xu & Jiménez 2022). The near-wall streamwise streaks are elongated small-scale structures. According to the instantaneous streamwise velocity, they can be divided into high-speed and low-speed steaks. They all have a common spanwise spacing of almost 100 wall units. As the Reynolds number becomes larger, large-scale motions (LSMs) and even VLSMs can be observed. These structures play a crucial role in momentum and energy transfer and interact with small-scale structures near the wall (Mathis *et al.* 2009; Ganapathisubramani *et al.* 2012; Hwang *et al.* 2016; Zhou *et al.* 2022). The hairpin packet is one of the extremely important LSMs. Adrian (2007) investigated the hairpin vortices in a turbulent boundary layer systematically and found that the streamwise length of the packets formed by 5–10 hairpins is approximately 2–3δ (δ indicates the boundary layer thickness). As for the VLSMs, their length can reach almost 30h (h indicates the channel half-height) in channel flows (Monty *et al.* 2007) and up to 10–15δ in turbulent boundary layers (Hutchins & Marusic 2007*b*). Hwang *et al.* (2016) distinguished the positive and negative u' structures and found that they possess different characteristics.

The Qs structures are another type of well-investigated coherent structures (Wark & Nagib 1991; Lozano-Durán *et al.* 2012; Lozano-Durán & Jiménez 2014; Chan & Chin 2022; Maeyama & Kawai 2023). Applying quadrant analysis to u' and v' (u' denotes the streamwise velocity fluctuation and v' the wall-normal velocity fluctuation), Q1 events (outward) with $u' > 0$, $v' > 0$, Q2 events (ejection) with $u' < 0$, $v' > 0$, Q3 events (inward) with $u' < 0$, $v' < 0$ and Q4 events (sweep) with $u' > 0$, $v' < 0$ are obtained. Lozano-Durán *et al.* (2012) identified the Qs structures and separated them into the attached and detached groups. The size, shape and spatial distribution of the individual structures are systematically investigated, and it is concluded that a pair of a sweep and an ejection with an associated vortex cluster between them is the predominant structure in the logarithmic layer. The ejections and sweeps contribute to almost 60 % of the tangential Reynolds stress. Lozano-Durán & Jiménez (2014) further studied the full-life evolution of Qs structures through a tracking method and pointed out that the attached Qs structures have the lifetime proportional to their distance from the wall. Recently, Maeyama & Kawai (2023) conducted simulations of flat plate through wall-modelled large-eddy simulation and they still got the ejection and sweep pairs by applying conditional average even though the structures are non-physically elongated from their simulation data.

In addition, research on coherent structures has also been extended to compressible wall-bounded flows (Smits *et al.* 1989; Ganapathisubramani, Clemens & Dolling 2006; Ringuette, Wu & Martín 2008; Pirozzoli & Bernardini 2011; Yao & Hussain 2020; Bross, Scharnowski & Kähler 2021; Chen *et al.* 2023; Zhang *et al.* 2023; Bai, Cheng & Fu 2024; Zhou *et al.* 2024). Compared with incompressible flows, the near-wall streaks in compressible flows are elongated due to density and temperature gradients (Coleman, Kim & Moser 1995) or cold isothermal wall conditions (Duan, Beekman & Martín 2010). Ringuette *et al.* (2008) studied the large-scale intense velocity fluctuation structures and reported that their average spanwise spacing is almost 0.5δ and some low-speed structures can have the streamwise length up to 100δ. Moreover, the scale of these structures suffers almost no compressibility effects (Williams *et al.* 2018; Cheng & Fu 2022). As for the Qs structures, Xu *et al.* (2021) found that the primary occurrences of Q1 and Q2 events are in the expansion regions, whereas Q3 and Q4 events are predominantly located in the compression regions near the wall in turbulent boundary layers with cold wall. This cold wall condition contributes to the enhancement of near-wall Q2 and Q3 events. However, the details of the individual structures have not been thoroughly investigated.

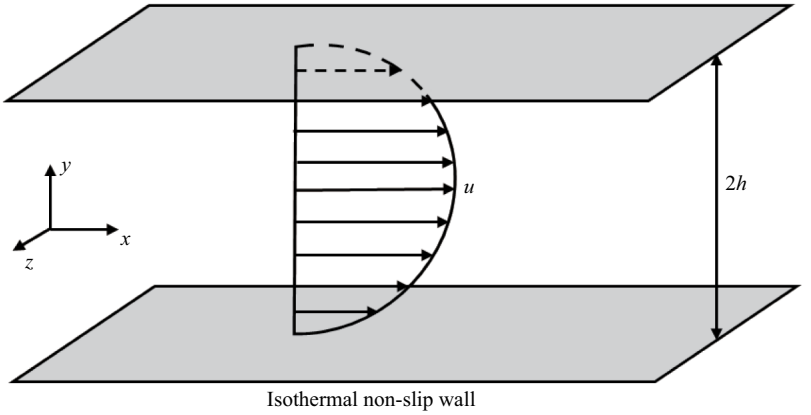

Figure 1. Diagram of the compressible turbulent channel flow model.

Until now, all these studies mentioned above are confined to the coherent structures of velocity. To inspect the relationship between velocity and temperature, the corresponding temperature structures should also be investigated. Existing literature on this subject is relatively scarce. Yuan *et al.* (2022) investigated the fluctuating temperature structures in supersonic turbulent boundary layers over cooled and heated walls. Bai *et al.* (2024) extracted the temperature structures following the popular Townsend's attached-eddy hypothesis (Townsend 1976) and inspected the inclination angles of these structures. The statistical similarity between the velocity and temperature structures was discovered. Moreover, the inner–outer interaction owned by velocity structures also exists between small- and large-scale temperature structures (Pirozzoli & Bernardini 2011). In addition, the heat flux structures were also investigated by Dong *et al.* (2022*a*, *b*) in compressible turbulent boundary layers and found heat flux structures show some asymmetrical characteristics compared with the shear stress structures.

In this work, the intense fluctuation structures and the Qs structures of both velocity and temperature will be investigated and compared with each other in the near-wall and outer regions by analysing the direct numerical simulation (DNS) database of compressible channel flows. In § 2, the database and the identification method will be introduced. In § 3, individual structures will be isolated so that the shape, size and other characteristics can be assessed. The Reynolds and Mach number effects will also be discussed. Then, the relationship between velocity and temperature will be carefully investigated from the instantaneous distribution, conditional average and the interscale energy transfer in § 4. Finally, the explanation of the identity and discrepancy between velocity and temperature structures will be provided in § 5.

2. The DNS database and identification of structures

2.1. *Database of compressible turbulent channel flows*

The database in this study contains five high-fidelity DNS cases of compressible turbulent channel flows driven by a volume force to maintain the constant mass flow rate. The physical model is displayed in figure 1. It should be mentioned that the averaged temperature is monotonically increasing from the wall to the channel centre, which is different from the boundary layer.

Case	Ma_b	Re_b	Re_τ	Re_τ^*	Δx^+	Δz^+	Δy^+_{min}	Δy^+_{max}
Ma15*Re*3K	1.5	3000	220	148	10.8	6.9	0.33	8.2
Ma15*Re*9K	1.5	9400	594	395	7.3	3.7	0.50	5.9
Ma15*Re*20K	1.5	20 020	1150	780	9.3	4.7	0.49	6.9
Ma30*Re*5K	3.0	4880	446	148	8.0	4.0	0.47	5.5
Ma30*Re*15K	3.0	15 000	1243	396	12.0	6.0	0.53	7.4

Table 1. Parameter settings of the DNS database. Here, Ma_b denotes the bulk Mach number, and Re_b, Re_τ, Re_τ^* denote the bulk Reynolds number, friction Reynolds number and semilocal friction Reynolds number, respectively. Additionally, Δx^+ and Δz^+ denote the streamwise and spanwise grid resolutions in viscous units, respectively, Δy^+_{min} and Δy^+_{max} denote the finest and coarsest resolution in the wall-normal direction.

The governing equations are shown as

$$\frac{\partial \rho}{\partial t} + \frac{\partial \rho u_j}{\partial x_j} = 0, \tag{2.1}$$

$$\frac{\partial \rho u_i}{\partial t} + \frac{\partial \rho u_i u_j}{\partial x_j} = -\frac{\partial p}{\partial x_i} + \frac{\partial \tau_{ij}}{\partial x_j} + f_1 \delta_{i1}, \tag{2.2}$$

$$\frac{\partial \rho E}{\partial t} + \frac{\partial \rho H u_j}{\partial x_j} = \frac{\partial \tau_{ij} u_i}{\partial x_j} - \frac{\partial q_j}{\partial x_j} + f_1 u_1, \tag{2.3}$$

where $x_i (i = 1, 2, 3) = (x, y, z)$, $u_i (i = 1, 2, 3) = (u, v, w)$ and

$$\tau_{ij} = \mu \left(\frac{\partial u_i}{\partial x_j} + \frac{\partial u_j}{\partial x_i} - \frac{2}{3} \frac{\partial u_k}{\partial x_k} \delta_{ij} \right), \quad q_j = -\kappa \frac{\partial T}{\partial x_j}. \tag{2.4a,b}$$

Here, t denotes time and u, v and w are the velocity components in the streamwise (x), wall-normal (y) and spanwise (z) directions, respectively. Here ρ, T, p represent density, temperature and pressure which satisfy the ideal gas law $p = \rho R T$, where R is the gas constant. Here $E = (1/2) u_i u_i + C_v T$ is the total energy and the total enthalpy is defined as $H = E + p/\rho$. Here τ_{ij} denotes the viscous stress, where μ is the dynamic viscosity obeying Sutherland's law, and q_j is the heat transfer term. Here f_1 is the body force. Additionally, the heat conductivity coefficient $\kappa = (C_p \mu)/Pr$. Here C_v and C_p stand for the constant-volume specific heat capacity and the constant-pressure specific heat capacity. The ratio of specific heat $\gamma = C_p/C_v = 1.4$ and the Prandtl number $Pr = 0.72$.

All these simulations are conducted in a computational domain of $4\pi h \times 2h \times 2\pi h$, where h is the half-height of the channel. The convection terms are discretized by a seventh-order hybrid scheme between weighted essentially non-oscillatory and a linear upwind-biased scheme, and an eighth-order central scheme is adopted for the discretization of viscous terms. Time advancement is carried out through the third-order Runge–Kutta scheme. Periodic boundary conditions are imposed in the streamwise and spanwise directions. The no-slip and isothermal conditions are adopted for upper and lower walls. The fidelity of these data has been validated in our previous work (Cheng & Fu 2022). Other parameters have been listed in table 1.

In this paper, $\bar{\varphi}$ denotes the Reynolds average of a generic variable φ and the corresponding fluctuation is φ', while the Favre average is $\tilde{\varphi} = \overline{\rho\varphi}/\bar{\rho}$ and the corresponding fluctuation is φ''. The friction velocity $u_\tau = \sqrt{\tau_w/\bar{\rho}_w}$ (where τ_w is the wall shear stress) and the viscous length scale $\delta_v = \bar{\mu}_w/(\bar{\rho}_w u_\tau)$. The variables normalized by wall units are denoted by a '+' superscript and the subscript 'b' and 'w' represent the bulk and wall values, respectively. For compressible flow, semilocal wall units are suitable to

Type	Intense fluctuation structures	Quadrant-event structures	Vortex structures
Velocity	$\lvert u'(\boldsymbol{x})\rvert > \alpha_u u'_{rms}(y)$	$\lvert u''(\boldsymbol{x})v''(\boldsymbol{x})\rvert > \alpha_{uv} u''_{rms}(y)v''_{rms}(y)$	$\Delta(\boldsymbol{x}) > \alpha_\Delta \Delta'_{rms}(y)$
Temperature	$\lvert T'(\boldsymbol{x})\rvert > \alpha_T T'_{rms}(y)$	$\lvert T''(\boldsymbol{x})v''(\boldsymbol{x})\rvert > \alpha_{Tv} T''_{rms}(y)v''_{rms}(y)$	Non

Table 2. Criteria for identifying different structures and α in each criterion is decided by percolation analysis. Here $\boldsymbol{x} = (x, z)$ and the subscript 'rms' denotes the root-mean-square of the variable.

investigate Reynolds number effects (Griffin, Fu & Moin 2021; Huang, Duan & Choudhari 2022) that are denoted by superscript '$*$', i.e. $u^*_\tau = \sqrt{\tau_w/\bar{\rho}}$ and $\delta^*_\nu = \bar{\mu}/(\bar{\rho}u^*_\tau)$. Thus, the semilocal friction Reynolds number $Re^*_\tau = h/\delta^*_\nu(h) = Re_\tau\sqrt{\bar{\rho}_c/\bar{\rho}_w}(\bar{\mu}_c/\bar{\mu}_w)$, where subscript '$c$' denotes the value of the variable at the channel centre.

2.2. *Identification of coherent structures*

The typical coherent structures, which include intense fluctuation structures for both u' and T', the Qs structures of tangential Reynolds stress $\widetilde{u''v''}$ and the corresponding heat flux $\widetilde{T''v''}$, are considered in this study as they are highly related to each other. It should be mentioned that for Qs structures, Favre fluctuations (defined based on the Favre average) are adopted to maintain consistency with the formulation in the transport equations. This choice has nearly no impact on the results, particularly when the Mach number is not high, as Cogo *et al.* (2022) reported. Fluctuation magnitudes are chosen as the criteria to identify these two structures. Moreover, the vortex structures for velocity field are also identified since they play an important role in the self-sustaining mechanism of wall turbulence (Toh & Itano 2005; Del Á lamo *et al.* 2006). To identify vortex structures, the Δ criterion is adopted since it does not depend on the divergence-free condition. Here Δ is the discriminant of the velocity gradient tensor $\boldsymbol{\nabla u}$ that can be calculated through three Galilean invariants of $\boldsymbol{\nabla u}$, written as

$$P = -\mathrm{tr}\,(\boldsymbol{\nabla u})\,, \quad Q = -\frac{1}{2}\left[\mathrm{tr}\big(\boldsymbol{\nabla u}^2\big) - \mathrm{tr}(\boldsymbol{\nabla u})^2\right], \quad R = -\det(\boldsymbol{\nabla u}). \tag{2.5a–c}$$

Then, Δ can be obtained through the following formula:

$$\Delta = \left(\frac{Q - P^2/3}{3}\right)^3 + \left(\frac{R + 2P^3/27 - PQ/3}{2}\right)^2. \tag{2.6}$$

Chong, Perry & Cantwell (1990) pointed out that in a vortex core, $\boldsymbol{\nabla u}$ is dominated by its rotational part that requires that Δ is positive.

The thresholds for these criteria are ambiguous and if wall turbulence is considered, its inhomogeneity in the wall-normal direction makes the problem more challenging. However, this study does not dig into it and different thresholds have been used at different (x, z)-planes according to their distance to the wall (Del Á lamo *et al.* 2006; Lozano-Durán *et al.* 2012; Hwang & Sung 2018*a*). Criteria for identifying all these structures are summarized in table 2. Percolation analysis is used to determine the thresholds α and the details can be found in the Appendix. It is found that all α can be set to 1.75 for all coherent structures in all cases except the vortex structures, which is the same value adopted by Lozano-Durán *et al.* (2012) in incompressible channel flow for tangential Reynolds stress. It was mentioned by both Lozano-Durán *et al.* (2012) and Hwang & Sung (2018*a*) that the results are qualitatively similar when α does not deviate much from 1.5. Meanwhile, the α_Δ for vortex structures is set as 0.1 according to the percolation analysis.

Since the domain is discretized by the Cartesian mesh, the mesh points, which meet the structure criterion, form a point set and the connected points are grouped into a subset which represents a single structure. However, structures obtained through this way will contain some meaningless fragments that only consist of several points due to numerical issues. Thus, in this study, only structures with volume larger than the cube of 30 wall units will be counted and analysed, as del Á lamo *et al.* (2006) suggested. The famous Townsend's attached-eddy model (Townsend 1976) provides an important perspective to inspect the features of coherent structures. Thus, the structures with their lowest parts below the first mesh node away from the wall are grouped into wall-attached structures. Otherwise, they will be regarded as wall-detached structures.

3. Characteristics of velocity and temperature structures

This section analyses the statistical characteristics of both intense fluctuation structures in § 3.1 and Qs structures in § 3.2 on velocity and temperature fields in all the five cases. Through this analysis, similarities and differences between these structures can also be identified. Each individual structure will be put into its circumscribing box with size $l_x \times l_y \times l_z$. The box extends from y_{min} to y_{max} in the wall-normal direction, and the height of the structure centre is y_c. The structure's volume is obtained by integration of the mesh points it contains, which is smaller than the total volume of the box. Moreover, the Reynolds and Mach number effects are also investigated by comparing all the cases.

3.1. *Intense fluctuation structures*

The intense fluctuation structures are identified by these two criteria:

$$\left|u'(\boldsymbol{x})\right| > 1.75u'_{rms}(y), \quad \left|T'(\boldsymbol{x})\right| > 1.75T'_{rms}(y). \tag{3.1a,b}$$

The numbers of structures used to accumulate statistics are more than 3×10^4 for low Reynolds number ($Re_b < 10^4$) cases and 10^5 for high Reynolds number ($Re_b \geqslant 10^4$) cases. According to the sign of the integral of fluctuations in one specific structure, structures can be divided into two categories, i.e. positive (+) and negative (–) dominant structures, which are not the same as the pure positive/negative structures in Hwang & Sung (2018*b*) and Yuan *et al.* (2022). However, the differences between them are slight. The comparison between these two methods has been conducted and the results (not shown in this paper) have only slight difference. Here, Case Ma30*Re*15K will be focused on first. Table 3 displays that the attached structures account for almost 70 % of the total structure volume statistically, though their number is much smaller than the detached ones. Similar results are also found by Hwang & Sung (2018*a*). The fractions of the positive and negative structures are also included in table 3. For attached structures, the same phenomenon that fewer negative structures account for larger volume can also be noticed. It should be mentioned that the intense T'^{-} structures get almost all the volume of attached T' structures, which means that the tall and large attached structures almost all belong to intense T'^{-} structures, while most of the attached intense T'^{+} structures are near wall with small volume. This phenomenon differs from that observed in compressible turbulent boundary layers with heated and slightly cooled walls (Yuan *et al.* 2022). In turbulent channel flow, the sole mechanism for transferring heat generated by viscous dissipation to the exterior is through the wall. Consequently, the temperature gradient near the wall is extremely steep. Given that the temperature increases monotonically from the wall towards the channel centre, the thermal condition can be analogized to that of an extremely cooled wall in a boundary layer. This unique characteristics of intense T' structures will

	Attached $u'(+,-)$	Detached $u'(+,-)$	Attached $T'(+,-)$	Detached $T'(+,-)$
Number fraction	0.21 (0.17, 0.05)	0.79 (0.34, 0.45)	0.26 (0.21, 0.05)	0.74 (0.20, 0.54)
Volume fraction	0.67 (0.18, 0.49)	0.33 (0.13, 0.19)	0.80 (0.01, 0.78)	0.20 (0.04, 0.16)

Table 3. The number and volume fractions of the intense fluctuation structures in Case Ma30Re15K. Two numbers in the brackets represent the fractions of positive structures and negative structures, respectively.

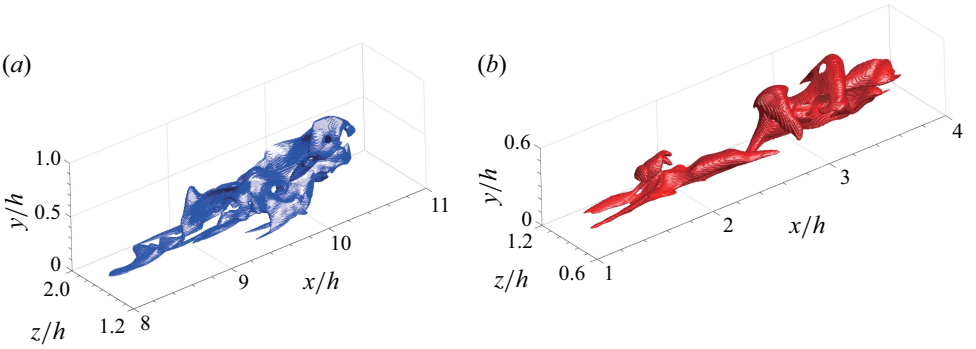

Figure 2. Samples of attached structures of (a) intense u' and (b) intense T'.

be investigated in § 4 carefully. Moreover, intense T' structures tend to be attached to the wall more than the intense u' structures.

3.1.1. *Attached structures*

The self-similarity of the attached structures, which has been verified by vast research in incompressible fields, will also be inspected in compressible channel flows here. Figure 2 depicts the extracted samples of attached structures from the instantaneous field of Case Ma30Re15K. Both the intense u' and T' structures extend from the wall to the central region of the channel, with lengths reaching approximately $3h$. It is noteworthy that the intense u' structures possess greater height and width in comparison with the T' structures.

The structure sizes are further investigated. Firstly, the joint probability density functions (p.d.f.s) of l_x and l_y are estimated as shown in figure 3. It is important to note that due to the relatively small number of large-scale structures in each instantaneous field, it is challenging to accumulate a sufficient number of large-scale structures comparable to the smaller ones. Consequently, the estimation uncertainty for the large-scale portion of the p.d.f.s may be greater than that for the smaller scales. However, the trend towards larger scales remains discernible. Lozano-Durán *et al.* (2012) and Hwang & Sung (2018*a*) provided the fitted equations $l_x^+ \approx 3l_y^+$ and $l_x^+ = 17.98(l_y^+)^{0.74}$, respectively, for attached structures in the logarithmic region. These two lines are also plotted in figure 3. Although the $Re_\tau = 1243$ in this case is not sufficiently high to encompass a very broad range of scales for LSMs and VLSMs, a linear relationship can still be observed when $l_y^+ > 100$. This observation aligns with the previously established relationship for both intense u' and T' structures. However, for this compressible case, the relation $l_x^+ \approx 7.5l_y^+$ is obtained, which exhibits a steeper slope compared (Lozano-Durán *et al.* 2012) with for Qs structures in incompressible flow. These results provide evidence for elongation of large-scale structures in compressible flow, which is also observed by Bross *et al.* (2021). Moreover, it can also be found that in the near-wall region ($l_y^+ < 50$), l_x primarily exhibits a

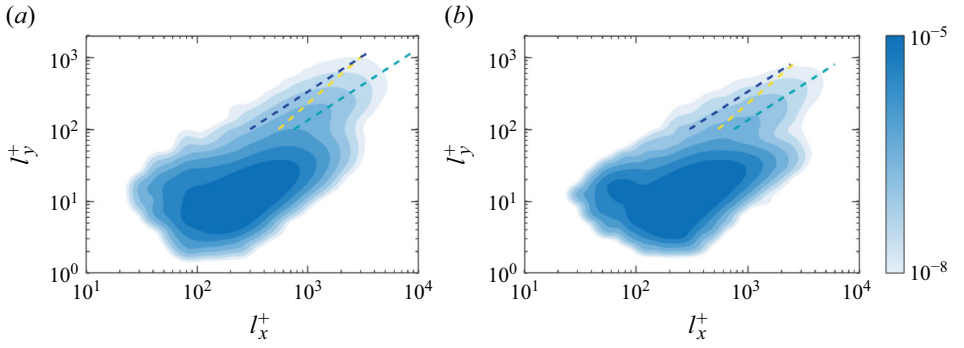

Figure 3. Joint p.d.f.s of the structure length and height for attached (*a*) intense u' structures and (*b*) intense T' structures. The yellow dashed line denotes $l_x^+ = 17.98(l_y^+)^{0.74}$ (Hwang & Sung 2018*a*), the blue dashed line stands for $l_x^+ \approx 3l_y^+$ (Lozano-Durán *et al.* 2012) and the green one, $l_x^+ \approx 7.5l_y^+$, is obtained in this paper. The contour levels are logarithmically distributed.

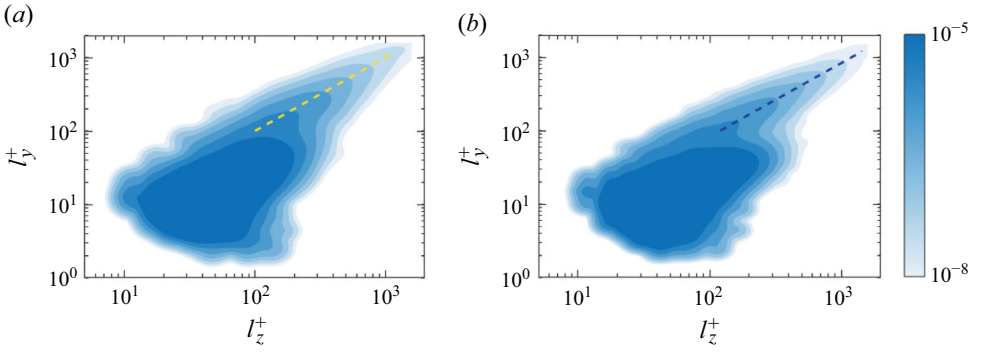

Figure 4. Joint p.d.f.s of the structure width and height for attached (*a*) intense u' structures and (*b*) intense T' structures. The yellow dashed line denotes $l_z^+ \approx l_y^+$, while the blue dashed line denotes $l_z^+ \approx 1.1l_y^+$. The contour levels are logarithmically distributed.

scale of $O(100)$ wall units, and these relations fail due to the significant influence of near-wall streaks. Subsequently, the width of the structures l_z is also taken into consideration, which is supposed to meet $l_z \approx l_y$ (Lozano-Durán *et al.* 2012; Hwang & Sung 2018*a*). The joint p.d.f.s of l_z and l_y with the equality relation are illustrated in figure 4. As the height of the structure increases, the width and height of the attached u' structures become nearly identical. However, it is observed that the attached T' structures are slightly stretched in the spanwise direction, with $l_z^+ \approx 1.1l_y^+$. Furthermore, the peak value of each p.d.f. is located around the position $(l_z^+, l_y^+) = (50, 15)$, which aligns with the width of the near-wall streaks. It should be mentioned that since the thermal wall condition of the compressible channel flow can be analogized to the extremely cooled wall of the boundary layer, near-wall coherent structures tend to elongate (Coleman *et al.* 1995; Duan *et al.* 2010). However, large-scale structures are almost unaffected by compressibility (Ringuette *et al.* 2008). Consequently, the lower part of the p.d.f.s shifts somewhat to the right compared with that in other compressible turbulent boundary layers with a not so cooled wall.

It can be seen that the attached intense T' structures exhibit the same self-similarity as the attached intense u' structures, based on the structure size. This observation provides a solid foundation for establishing the relation between u'_{rms}- and T'_{rms}-like SRA, since the attached structures account for nearly 70 % of the total structure volume.

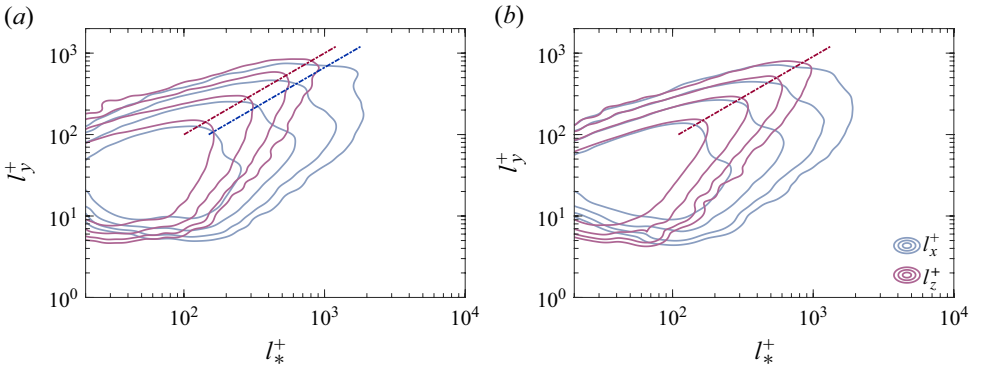

Figure 5. Joint p.d.f.s of the structure height and another dimension for detached (*a*) intense u' structures and (*b*) intense T' structures. The red line denotes $l_*^+ \approx l_y^+$ and the blue line denotes $l_*^+ \approx 1.5l_y^+$, where subscript '$*$' can be x or z. The contour levels are logarithmically distributed.

3.1.2. *Detached structures*

The detached structures constitute a significant proportion of numbers, exceeding 70 %, yet they account for less than one-third of the total structural volume. The length, width and height of detached structures are almost at the same scale (Lozano-Durán *et al.* 2012). It turns out that the results for the intense T' structures remain the same, which also has $l_x^+ \approx l_y^+ \approx l_z^+$ in this case, as illustrated in figure 5(*b*). However, the length of the detached intense u' structures is slightly elongated in the streamwise direction, reaching approximately $1.5l_y^+$. It can be concluded that the streamwise stretching of intense u' fluctuation structures consistently occurs in compressible channel flows. Moreover, the width of these structures remains close to their height, regardless of whether they are attached or detached. Although the detached intense T' structures exhibit slightly different features compared with the intense u' structures, the relatively small volume of the detached T' structures renders this discrepancy acceptable when establishing an analogy between u'_{rms} and T'_{rms}.

3.2. *The Qs structures*

Quadrant events, particularly Q$^-$s (Q2s and Q4s), play a crucial role in the transfer and redistribution of momentum and energy within wall-bounded turbulent flows. Herein, the Qs structures are identified based on the following criteria:

$$\left|u''(\boldsymbol{x})v''(\boldsymbol{x})\right| > 1.75u''_{rms}(y)v''_{rms}(y), \quad \left|T''(\boldsymbol{x})v''(\boldsymbol{x})\right| > 1.75T''_{rms}(y)v''_{rms}(y). \quad (3.2a,b)$$

For Case Ma15*Re*3K, over 6×10^4 structures are utilized for statistical accumulation, while more than 10^5 are used for other cases. Table 4 presents the number and volume fractions of Q1s–Q4s structures for both $u''v''$ and $T''v''$. The attached structures are counted separately. Unlike the intense fluctuation structures, the total volume used to calculate the volume fractions for Qs structures is based on the entire channel volume. Results show that the volume fractions for Qs structures of $u''v''$ are almost consistent with the results reported by Lozano-Durán *et al.* (2012) in incompressible flows with $Re_\tau = 950$. The Q$^-$s structures surpass the Q$^+$s structures (Q1s and Q3s) in both number and volume. In this study, we focus exclusively on the Q$^-$s structures. It is evident that the volumes of the attached Q2s structures are more than three times larger than the attached Q4s structures, indicating that the predominant phenomenon in this case involves ejections, which transfer momentum and energy from the near-wall region to the outer region.

	N_1	N_2	N_3	N_4	V_1	V_2	V_3	V_4
All $u''v''$	0.19	0.25	0.30	0.27	0.004	0.059	0.005	0.026
Attached $u''v''$	0.01	0.07	0.05	0.04	0.000	0.041	0.000	0.012
All $T''v''$	0.09	0.28	0.40	0.24	0.001	0.082	0.009	0.006
Attached $T''v''$	0.02	0.07	0.06	0.05	0.000	0.068	0.000	0.002

Table 4. The number and volume fractions of the Qs structures in Case Ma30Re15K. Here $N_1 - N_4$ denote the number fractions for Q1s–Q4s structures, respectively. Here $V_1 - V_4$ denote the volume fractions with respect to the whole channel volume for Q1s–Q4s structures, respectively.

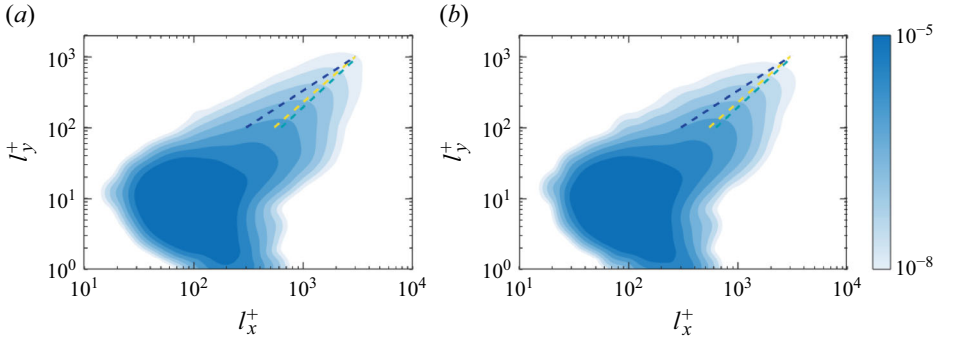

Figure 6. Joint p.d.f.s of the structure length and height for attached Qs structures of (*a*) $u''v''$ and (*b*) $T''v''$. The yellow dashed line denotes $l_x^+ = 17.98(l_y^+)^{0.74}$ (Hwang & Sung 2018*a*), the blue dashed line stands for $l_x^+ \approx 3l_y^+$ (Lozano-Durán *et al.* 2012) and the green one, $l_x^+ \approx 25(l_y^+)^{0.7}$, is obtained in this paper. The contour levels are logarithmically distributed.

Furthermore, the volume fraction of Q4s structures for $T''v''$ is extremely low, whereas the Q2s structures are significantly larger. This observation aligns with the findings in § 3.1, as less intense T'^+ structures directly contribute to fewer Q1s and Q4s structures, which possess positive temperature fluctuation components. This represents a notable distinction between streamwise velocity and temperature, a topic that will be further explored in § 4.

3.2.1. *Attached structures*

The size distributions of attached Qs structures are first examined, and the joint p.d.f.s of the structure height and its other two dimensions are presented in figures 6 and 7. The Qs structures for $u''v''$ and $T''v''$ exhibit nearly identical sizes statistically, as indicated by the p.d.f.s, except that the original equality between structure width and height transitions into a slightly nonlinear relationship for $T''v''$ structures which is expressed as $l_z^+ \approx 1.6(l_y^+)^{0.95}$, as shown in figure 7(*b*). In comparison with the intense fluctuation structures discussed in § 3.1, Qs structures have a greater number of flat streaks with heights of $O(1)$ wall units, since a turning point exists as l_y^+ approaching unity in figure 6. Furthermore, the fitted equation obtained in this study for the length and height of Qs structures when $l_y^+ > 100$ is given by $l_x^+ \approx 25(l_y^+)^{0.7}$, which aligns more closely with the findings reported in Hwang & Sung (2018*a*). They attributed the deviation from linearity to the inclination and meandering of the structures, as well as the relatively low Reynolds number ($Re_\tau \approx 1000$). However, this phenomenon will not be further explored in the present study, as the focus is primarily on the relationship between velocity and temperature coherent structures. The high degree of similarity in size between the attached

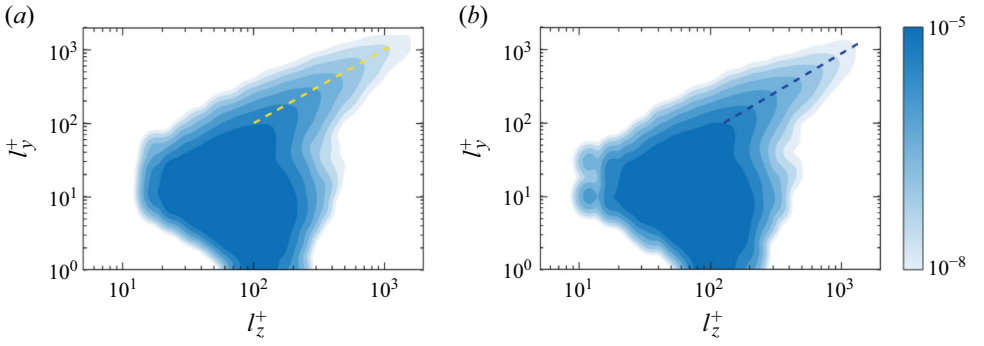

Figure 7. Joint p.d.f.s of the structure width and height for attached Qs structures of (*a*) $u''v''$ and (*b*) $T''v''$. The yellow dashed line denotes $l_z^+ \approx l_y^+$, while the blue dashed line denotes $l_z^+ \approx 1.6(l_y^+)^{0.95}$. The contour levels are logarithmically distributed.

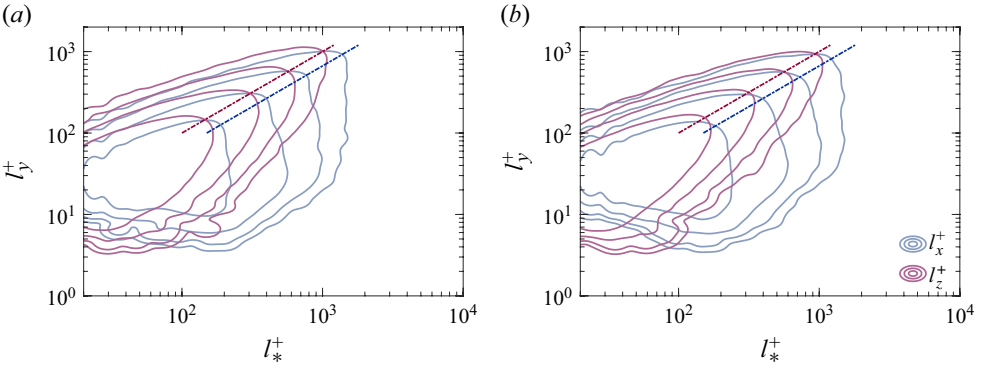

Figure 8. Joint p.d.f.s of the structure height and another dimension for detached Qs structures of (*a*) $u''v''$ and (*b*) $T''v''$. The red line denotes $l_*^+ \approx l_y^+$ and the blue line denotes $l_*^+ \approx 1.5l_y^+$, where subscript '$*$' can be x or z. The contour levels are logarithmically distributed.

Qs structures of $u''v''$ and $T''v''$ suggests the existence of similar momentum and energy transport results in compressible turbulent flows.

3.2.2. *Detached structures*

The size of the detached Qs structures is also studied by estimating the joint p.d.f.s across different dimensions. The results are illustrated in figure 8. The elongation in streamwise direction persists for detached Qs structures in this compressible flow case, with the dimensional relationship given as $l_x^+ \approx 1.5l_y^+ \approx 1.5l_z^+$. Unlike the intense fluctuation structures, no significant discrepancy is observed between figures 8(*a*) and 8(*b*). To date, it has been found that both the attached and detached Qs structures exhibit negligible difference between $u''v''$ and $T''v''$. Therefore, it is reasonable to anticipate that the turbulent Prandtl number Pr_t, which characterizes the relationship between the averaged Reynolds shear stress $\widetilde{u''v''}$ and averaged heat flux $\widetilde{T''v''}$, will have a value close to unity, with deviations only in the extremely near-wall region.

3.3. *Reynolds and Mach numbers effects*

All five cases are analysed to investigate the Reynolds and Mach number effects on both velocity and temperature structures. The semilocal friction Reynolds number Re_τ^*

Cases	Re_τ^*	u'	u'^+	u'^-	u'^-_{att}	T'	T'^+	T'^-	T'^-_{att}
Ma15*Re*3K	148	0.072	0.016	0.056	0.036	0.078	0.005	0.073	0.057
Ma15*Re*9K	395	0.075	0.023	0.052	0.029	0.066	0.006	0.060	0.040
Ma15*Re*20K	780	0.073	0.022	0.051	0.036	0.109	0.002	0.108	0.096
Ma30*Re*5K	148	0.078	0.017	0.061	0.045	0.066	0.007	0.059	0.043
Ma30*Re*15K	396	0.082	0.026	0.056	0.040	0.084	0.005	0.079	0.066

Table 5. The volume fractions of different intense fluctuation structures with respect to the whole channel in all five cases. Here Re_τ^* is the semilocal friction Reynolds number. Subscript '*att*' represents the attached structures.

is selected as the indicator. The analysis proceeds in an orderly manner, first examining intense fluctuation structures followed by Qs structures. It should be mentioned that the subsequent analysis in this chapter remains relatively preliminary and more cases with higher Mach and Reynolds numbers should be inspected to make the conclusions more solid in the future works.

3.3.1. *Intense fluctuation structures*

Table 5 lists the volume fractions of different structures with respect to the whole channel. It can be found that, except for the intense u'^- structures whose volume fractions decrease monotonically with increasing Reynolds number in both Mach 3 and Mach 1.5 cases, the Reynolds number effects on other structures are non-monotonic. Furthermore, the influence of the Reynolds number varies depending on the Mach numbers, particularly for intense T' structures. Consequently, the Reynolds number effects cannot be discussed separately without considering the Mach number. Additionally, a higher Mach number generally leads to larger volume fractions for almost all u' structures and a greater proportion of attached components in negative structures. However, the combined influence of Reynolds and Mach numbers on the volume of T' structure is highly complex and requires further investigation. Notably, the volume fractions for T'^+ structures remain small regardless of the Reynolds and Mach numbers, which is a remarkable difference in comparison with the u' structures. This observation suggests that the temperature fluctuations exhibit negative skewness.

Structure sizes are evaluated based on aspect ratios. The p.d.f.s of the length-to-height and width-to-height ratio are presented in figures 9 and 10, respectively. Given the distinct characteristics of attached and detached structures, estimations are performed separately for these two types. The elongation of the attached structures in the streamwise direction, as § 3.1 mentioned, can also be observed in figure 9. In contrast, detached structures exhibit isotropic features. The variation of the l_x/l_y for detached structures exhibits no clear trend as the Reynolds and Mach numbers change. The peak values for all lines are located around $l_x/l_y = 1$ for u' structures and $l_x/l_y = 0.9$ for T' structures. However, it is also observed that the distributions of l_x/l_y for detached u' structures in the two cases with lowest $Re_\tau^* = 148$ deviate from the other three cases near the peak, as shown in figure 9(*a,b*). Therefore, the length-to-height ratio of detached intense fluctuation structures can achieve a fully developed state when the Reynolds number reaches a specific threshold. Regarding attached structures, it is worth noting that most attached structures with $l_x/l_y > 20$ have heights exceeding 100 wall units, which are regarded as large structures here. On the contrary, small structures with heights less than 100 wall units dominate the range $l_x/l_y < 3$. The dashed lines in figure 9 exhibit a relatively flat plateau when l_x/l_y falls within the range of $3 - 20$. This plateau is flatter for u' structures. Furthermore, focusing

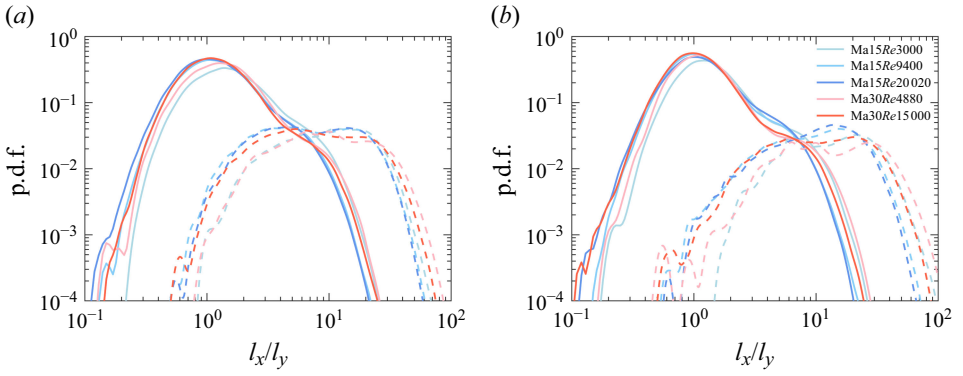

Figure 9. The p.d.f.s of the length-to-height ratio for intense fluctuation structures of (*a*) u' and (*b*) T'. Here —— denotes detached structures and - - - - denotes attached structures.

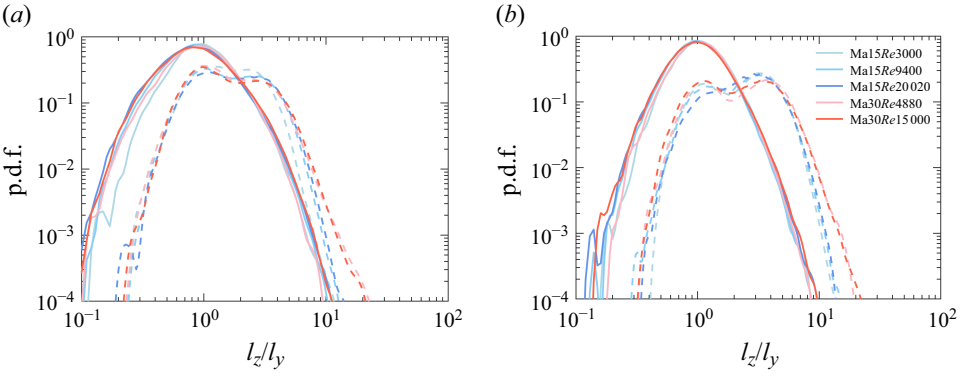

Figure 10. The p.d.f.s of the width-to-height ratio for intense fluctuation structures of (*a*) u' and (*b*) T'. Here —— denotes detached structures and - - - - denotes attached structures.

on the large structures, higher Mach numbers or smaller Reynolds numbers result in more highly elongated structures. However, the volume of these highly elongated structures cannot be excessively large, as their height must remain small enough to achieve the large elongation rate.

The width remains relatively small since the dashed lines in figure 10 have the similar plateau when l_z/l_y is between 1 and 4. Unlike the elongation in the streamwise direction, the stretch in the spanwise direction is only sensitive to the Mach number. As the Mach number increases, the number of extremely stretched structures also increases. Comparing the attached u' structures with attached T' structures, it can be noticed that the l_z/l_y of T' structures tends to be slightly larger according to the location of the peak. However, for both detached u' and T' structures, the collapse behaviour is consistent across all cases when $l_z/l_y > 0.6$ despite the variations in Reynolds and Mach numbers.

3.3.2. *The Qs structures*

The Reynolds and Mach number effects on Q^-s structures are investigated, since these structures play an important role in turbulence momentum and energy transport. The volume fractions of different types of Q^-s structures are summarized in table 6. For Qs structures of both $u''v''$ and $T''v''$, the Reynolds number effects exhibit a non-monotonic

Cases	Re^*_τ	$(Q^-s)_u$	$(Q2s)_u$	$(Q4s)_u$	$(Q2s)_{att,u}$	$(Q^-s)_T$	$(Q2s)_T$	$(Q4s)_T$	$(Q2s)_{att,T}$
Ma15*Re*3K	148	0.083	0.069	0.014	0.052	0.082	0.075	0.007	0.060
Ma15*Re*9K	395	0.084	0.060	0.024	0.043	0.073	0.065	0.009	0.049
Ma15*Re*20K	780	0.086	0.063	0.023	0.052	0.107	0.103	0.009	0.093
Ma30*Re*5K	148	0.080	0.061	0.019	0.046	0.068	0.059	0.006	0.048
Ma30*Re*15K	396	0.085	0.059	0.026	0.041	0.088	0.082	0.006	0.068

Table 6. The volume fractions of different Qs structures with respect to the whole channel in all the five cases. Here Re^*_τ is the semilocal friction Reynolds number. The subscript 'u' denotes structures of $u''v''$, 'T' denotes structures of $T''v''$ and 'att' represents the attached structures.

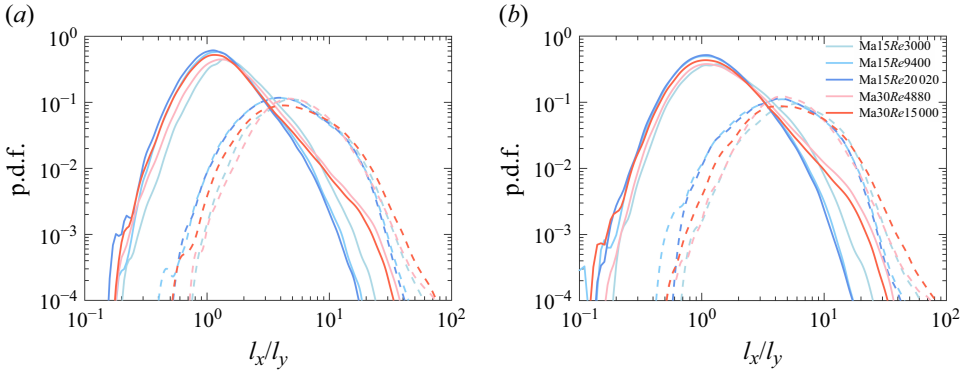

Figure 11. The p.d.f.s of the ratio of length to height for Qs structures of (*a*) $u''v''$ and (*b*) $T''v''$. Here —— denotes detached structures and - - - - denotes attached structures.

behaviour, but the latter ones are more sensitive. Furthermore, it is observed that the response of $u''v''$ and $T''v''$ Q$^-$s structures to the variations in Mach number differs. Specifically, Cases Ma15*Re*9K and Ma30*Re*15K exhibit nearly identical volume fractions for Q$^-$s structures $u''v''$ regardless of type, whereas distinct Mach numbers lead to markedly different volume fractions for Q2s structures of $T''v''$. Therefore, the energy transfer is strongly correlated with the Mach number. Additionally, similar to intense fluctuation structures, the Q4s structures of $T''v''$ with $T' > 0$ account for only a small proportion of the total channel volume compared with those of $u''v''$.

Structure sizes of all the Qs structures are also examined, and distinct behaviours are identified in comparison with the intense fluctuation structures. Figure 11 illustrates the p.d.f.s of length-to-height ratio. A higher Mach number can still induce stronger elongation in the streamwise direction, with the effects being significantly more pronounced here than in § 3.3.1. Furthermore, the plateau observed in the dashed line in figure 9 is now replaced by a peak in figure 11. No noticeable difference is found between Qs structures of $u''v''$ and $T''v''$.

Although the width-to-height ratio of the detached Qs structures is insensitive to both Reynolds and Mach numbers, as evidenced by the good collapse of lines in figure 12, the Mach number effects on attached Qs structures are extremely notable. A large number of attached Qs structures with l_z/l_y around 10 are generated in the cases at Mach 3. Upon closer examination, these structures predominantly reside in the near-wall region with $y^+_{max} < 30$. Furthermore, among these wide structures in Case Ma30*Re*15K, Q3s structures account for 50 % of the volume, whereas the proportion of Q2s is 34 %.

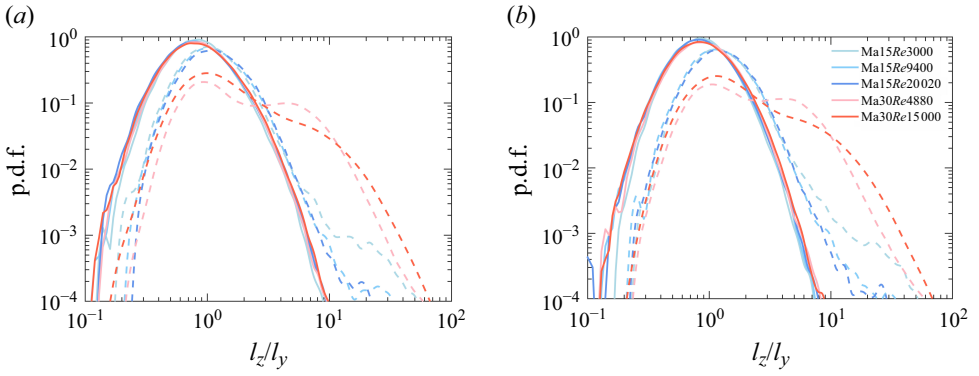

Figure 12. The p.d.f.s of the ratio of width to height for Qs structures of (*a*) $u''v''$ and (*b*) $T''v''$. Here —— denotes detached structures and - - - - denotes attached structures.

4. Relationship between streamwise velocity and temperature fluctuations

In this section, the relation between the streamwise velocity and temperature fluctuations will be thoroughly investigated. The governing equations of streamwise velocity and temperature with the transport equation of a passive scalar in channel flows φ are presented here for comparison,

$$\frac{\partial \rho u}{\partial t}+\frac{\partial \rho u_j u}{\partial x_j}=\frac{\partial}{\partial x_j}\left(\mu\frac{\partial u}{\partial x_j}\right)+\frac{\partial}{\partial x_j}\left[\mu\left(\frac{\partial u_j}{\partial x}-\frac{2}{3}\frac{\partial u_i}{\partial x_i}\delta_{1j}\right)\right]-\frac{\partial p}{\partial x}+f_1, \tag{4.1}$$

$$\frac{\partial \rho T}{\partial t}+\frac{\partial \rho u_j T}{\partial x_j}=\frac{\partial}{\partial x_j}\left(\frac{\kappa}{C_v}\frac{\partial T}{\partial x_j}\right)-\frac{p}{C_v}\frac{\partial u_j}{\partial x_j}+\frac{\tau_{ij}}{C_v}\frac{\partial u_i}{\partial x_j}, \tag{4.2}$$

$$\frac{\partial \rho \varphi}{\partial t}+\frac{\partial \rho u_j \varphi}{\partial x_j}=\frac{\partial}{\partial x_j}\left(\lambda\frac{\partial \varphi}{\partial x_j}\right)+\theta, \tag{4.3}$$

where λ is the diffusivity of the scalar, which is related to the viscosity via the Schmidt number $Sc=\mu/(\rho\lambda)$ and θ is the source term introduced to prevent a uniform field solution. The corresponding sources in the other two equations are the volume force f_1 and the dissipation term $\tau_{ij}(\partial u_i/\partial x_j)$. For compressible flow, the velocity divergence does not vanish, and additional terms remain in (4.1) and (4.2). In the near-wall region, the convection term can be neglected since the convection velocity is quite small. Thus, the distribution of a specific variable is primarily determined by the terms on the right-hand side of its governing equation. Cheng & Fu (2024) conducted a detailed investigation into the multiphysics couplings between these variables in the spectral domain and reported that the viscous term associated with the velocity divergence in (4.1) only leads to different intermittent behaviours. Thus, with same form of Laplace and source terms, streamwise velocity exhibits quite similar behaviours to the passive scalar. Although the source term in governing equation (4.2) for temperature is not a constant in the wall-normal direction as in the other two equations, Cheng & Fu (2024) mentioned that the temperature can be roughly treated as a passive scalar in most region of the channel after inspecting its spectral behaviours, which indicates that the form of the source term does not matter much for the low-order statistical characteristics. Therefore, the high correlations between streamwise velocity and temperature fluctuations can be anticipated in the near-wall region.

The above analysis can be proven by the one-point correlation of u' and T', as shown in figure 13. The channel can be divided into two regions which are separated by the x–z plane at $y^+=50$. Below this plane, u' and T' are highly correlated with each other.

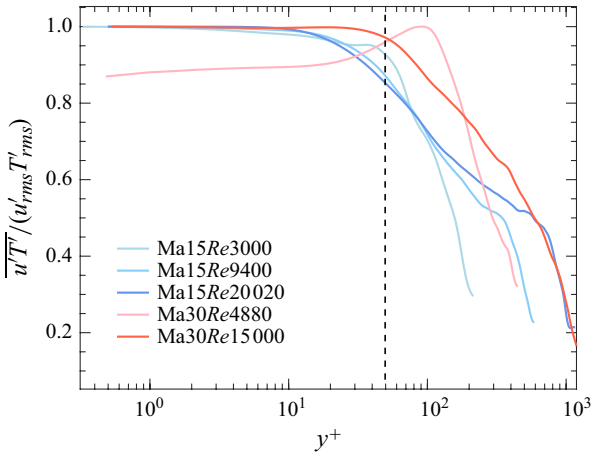

Figure 13. Correlations of velocity fluctuations and temperature fluctuations normalized by their root-mean-square. The dashed line denotes $y^+ = 50$.

However, the correlation drops rapidly in the logarithmic region, which indicates that the streamwise velocity obeys a different mechanism compared with temperature. One possible reason is that in the logarithmic region, the convection term plays the leading role and the high nonlinearity of it in (4.1) shows up. In this section, another detailed explanation from the perspective of coherent structures will be introduced.

4.1. *Overlapping structures*

Since all structures are extracted separately, their instantaneous distributions and shapes can be systematically compared one by one between the streamwise velocity and temperature to identify their similarities and differences. Turbulence is an extremely complicated system, and the instantaneous behaviours between two different variables are unlikely to exhibit high similarity without some form of average operation, such as root-mean-square. However, this approach can provide rich details. In this paper, the structures (remarked as s_i) of a specific variable are extracted and grouped into a structure set S. Each s_i consists of a mesh point set P_i which is decided by the method introduced in § 2.2. A significant degree of overlap between the structures of streamwise velocity and temperature indicates that these paired structures occupy nearly identical spatial position with similar shapes. To obtain a quantitative result, the overlap ratio for two structures is defined as

$$D_{i,j} = 2\frac{|\{P_i\}_{S_1} \cap \{P_j\}_{S_2}|}{|\{P_i\}_{S_1}| + |\{P_j\}_{S_2}|}. \tag{4.4}$$

Here, S_1 and S_2 are structure sets corresponding to two distinct variables and $|\cdot|$ denotes the cardinality of the set, specifically referring to the number of mesh points here. If $D_{i,j} > D_{cr}$, the ith structure in S_1 and the jth structure in S_2 are identified as an overlapping pair. A higher value of $D_{i,j}$ indicates a larger common part between the two structures. To ensure that no single structure is assigned to more than one overlapping pair, D_{cr} is set to 50 %. Structures within the same overlapping pairs are located at nearly identical spatial positions. With this criterion, the spatial distributions of the intense fluctuation structures and Qs structures for streamwise velocity and temperature are compared with each other in details.

Cases	Re_τ^*	$2N_{o,1}/N_{u+T,1}$	$2V_{o,1}/V_{u+T,1}$	$2N_{o,2}/N_{u+T,2}$	$2V_{o,2}/V_{u+T,2}$
Ma15*Re*3K	148	72 59 %	55.50 %	10.68 %	22.96 %
Ma15*Re*9K	395	63.35 %	46.28 %	4.80 %	3.47 %
Ma15*Re*20K	780	58.49 %	40.64 %	3.81 %	0.60 %
Ma30*Re*5K	148	67.91 %	61.27 %	14.71 %	28.87 %
Ma30*Re*15K	396	60.16 %	47.22 %	8.33 %	2.61 %

Table 7. The number (N) and volume (V) fractions of the overlapping pairs between intense u' and T' structures. Here Re_τ^* is the semilocal friction Reynolds number. Subscript 'o' denotes the overlapping pairs, 'u+T' denotes the summation of the variables of intense u' and T' structures and '1', '2' denote the regions with $y^+ < 50$ and $y^+ > 50$, respectively. Specifically, V_o is the volume of the common parts in overlapping pairs.

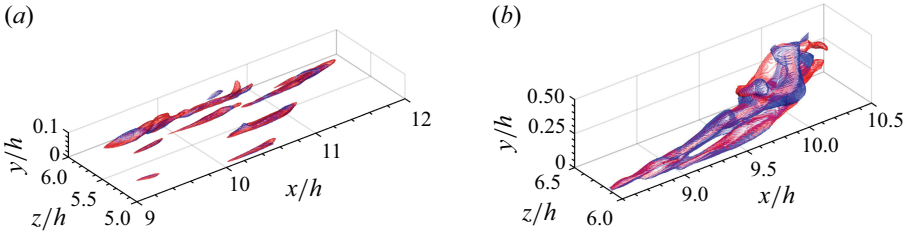

Figure 14. Samples of overlapping pairs in regions with (*a*) $y^+ < 50$ and (*b*) $y^+ > 50$ for Case Ma30*Re*15K. Red and blue structures denote intense u' and T' structures, respectively.

4.1.1. *Intense fluctuation structures*

Table 7 lists the detailed information on the overlapping pairs, including their numbers and volume fractions with respect to all intense fluctuation structures in regions with $y^+ < 50$ and $y^+ > 50$, separately. It is remarkable that both the number and volume fractions of the overlapping pairs are significantly high when $y^+ < 50$. For the instantaneous field, it is surprising that more than half of the intense u' and T' structures are positioned nearly identically, which gives the reason for the high correlation in the near-wall region in figure 13. This observation is consistent with the analysis from the governing equations that both the streamwise velocity and temperature exhibit behaviours akin to passive scalar. As the height increases, their instantaneous positions diverge completely. Additionally, at higher Reynolds numbers, the intense u' and T' structures exhibit reduced overlap. Therefore, identifying the characteristics (e.g. shape) of the overlapping pairs is essential for uncovering the underlying mechanisms.

Figure 14 presents the typical overlapping pairs at two height regions for Case Ma30*Re*15K. Both the near-wall streaks and large-scale structures exhibit high overlapping rates. A further analysis is conducted by inspecting the volume-weighted averages of the intense u' structures within the overlapping pairs (which are quite similar for intense T' structures) through the following formula:

$$[l] = \left(\sum_i V_i l_i\right) \Big/ \sum_i V_i, \tag{4.5}$$

where l is a specific variable, V denotes the volume of velocity structure, subscript 'i' denotes the ith overlapping pair, and '[ ]' denotes the average operation. Table 8

Cases	$\left[l^+_{x,1}\right]$	$\left[l^+_{y,1}\right]$	$\left[l^+_{z,1}\right]$	$\left[l^+_{x,2}\right]$	$\left[l^+_{y,2}\right]$	$\left[l^+_{z,2}\right]$
Ma15*Re*3K	905	82	107	2225	266	326
Ma15*Re*9K	722	81	114	2609	376	382
Ma15*Re*20K	692	80	120	1474	217	232
Ma30*Re*5K	1511	91	161	4775	559	694
Ma30*Re*15K	1356	98	187	4379	560	605

Table 8. The volume-weighted average of the intense u' structures in the overlapping pairs. Here '[ ]' denotes the average operation weighted by the volume of the circumscribing box of a specific structure and '1', '2' denote the regions with $y^+ < 50$ and $y^+ > 50$, respectively.

summarizes the results. It shows that the near-wall overlapping pairs mainly consist of streamwise streaks, whereas the overlapping pairs of large-scale structures play a more significant role in sustaining the correlation in the outer region. Since the existence of these streaks constitutes a fundamental process in the self-sustaining cycle of turbulence (Toh & Itano 2005; Del Á lamo *et al.* 2006), the high overlapping rate between the instantaneous streaks of u' and T' also suggests that the temperature passively follows the self-sustaining cycle of velocity. Furthermore, the observed difference may result from the discrepancy of the large-scale structures in the outer layer through the inner–outer interaction, which has been widely reported by many researchers. Particularly in the high Reynolds number cases, where the number and effects of large-scale structures become considerable, the overlapping rate is extremely low, indicating that the kinetic processes of the LSMs and VLSMs for velocity and temperature have different mechanisms. These mechanisms will be further investigated in §§ 4.2 and 4.3.

Therefore, in the near-wall region, the similar diffusive feature, which is dominant in their governing equations (4.1) and (4.2), reflects in the similar kinematics behaviours between streamwise velocity and temperature, such as the overlapping streaks structures. The discrepancy in the skewness of their fluctuations may ascribe to the interactions with outer layer and different wall-normal distributions of the source terms. However, the highly nonlinear advection term in (4.1) begins to take effects in the logarithmic and outer regions, reducing the correlation between streamwise velocity and temperature. The remaining overlapping pairs likely originate from the near-wall region, which is associated with momentum and energy transfer in the channel and will be further discussed in § 4.1.2.

4.1.2. *The Qs structures*

The overlapping pairs of Qs structures of streamwise velocity and temperature are inspected, as they provide an important perspective for investigating momentum and energy transfer in turbulent flow. Table 9 presents the details about the overlapping pairs, including their number and volume fractions with respect to all Qs structures in the regions with $y^+ < 50$ and $y^+ > 50$ separately. The results exhibit strong resemblance to intense fluctuation structures in the near-wall region, as shown in table 7, while the volume fractions are higher in the outer layer. A negative correlation between the overlapping rate and the Reynolds number can also be found here. Furthermore, it also indicates that the instantaneous distributions of the large-scale Qs structures of $u''v''$ and $T''v''$, which play a more critical role in cases with higher Reynolds number, are totally different.

Cases	Re_τ^*	$2N_{o,1}/N_{uv+Tv,1}$	$2V_{o,1}/V_{uv+Tv,1}$	$2N_{o,2}/N_{uv+Tv,2}$	$2V_{o,2}/V_{uv+Tv,2}$
Ma15Re3K	148	65.68 %	54.52 %	14.76 %	26.94 %
Ma15Re9K	395	60.24 %	49.03 %	8.93 %	14.97 %
Ma15Re20K	780	57.81 %	45.72 %	7.80 %	3.52 %
Ma30Re5K	148	77.84 %	57.12 %	18.12 %	34.37 %
Ma30Re15K	396	68.61 %	55.14 %	11.72 %	9.71 %

Table 9. The number (N) and volume (V) fractions of the overlapping pairs between Qs structures of $u''v''$ and $T''v''$. Here Re_τ^* is the semilocal friction Reynolds number. Subscript 'o' denotes the overlapping pairs, 'uv+Tv' denotes the summation of the variables of Qs structures of $u''v''$ and $T''v''$ and '1', '2' denote the regions with $y^+ < 50$ and $y^+ > 50$, respectively. Specially, V_o is the volume of the common parts in overlapping pairs.

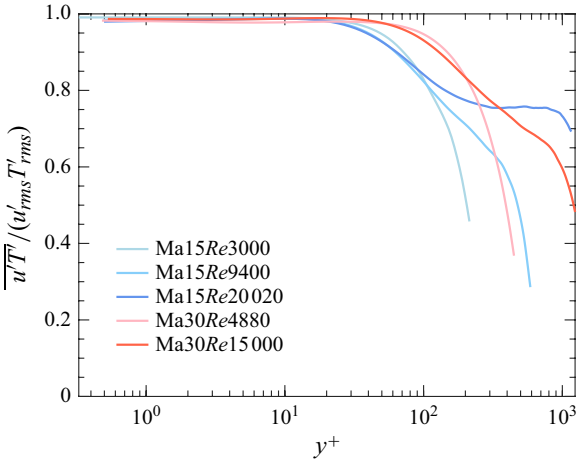

Figure 15. Correlations of velocity fluctuations and temperature fluctuations in overlapping pairs of Q2s structures normalized by their root-mean-square.

The correlation between streamwise velocity and temperature fluctuations is examined within the overlapping pairs of Q2s structures to investigate the transport of these fluctuations from the near-wall region to the outer layer. Figure 15 demonstrates high correlations, particularly for high Reynolds number cases, across nearly the entire domain except near the channel centre. The Reynolds and Mach numbers effects are also notable. Higher Mach numbers lead to a broader range of tight correlations, whereas higher Reynolds number enhance the correlation in the outer layer. Therefore, the overlapping ejection-event structures serve as one of the sources contributing to the remaining correlation of u' and T' in the outer layer. However, the effects of the highly nonlinear advection term in (2.2) diminishes the correlation progressively. Further discussion on these influences, arising from the different forms of governing equations in the outer layer, will be presented in subsequent parts from the perspective of self-similarity of the coherent structures.

4.2. *Conditional average*

The size of intense fluctuation structures for the u' and T' has been investigated in § 3. Here, the shapes of the attached u' and T' structures are analysed in conjunction with the

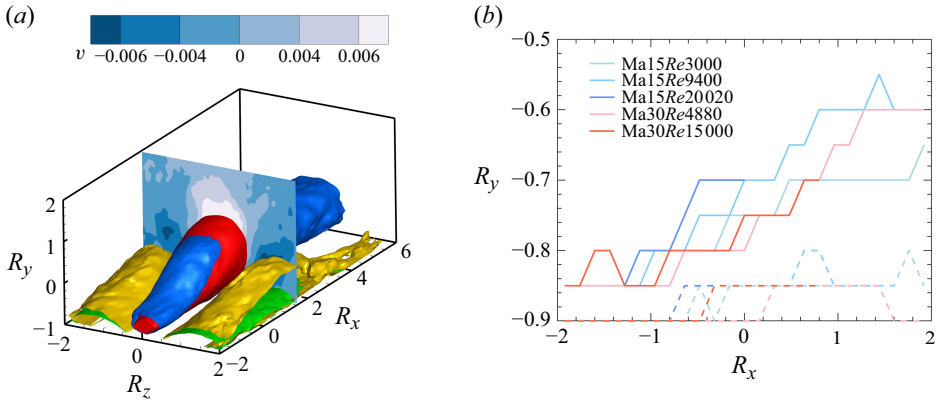

Figure 16. (*a*) Three-dimensional plot of the average velocity and temperature fluctuation fields conditioned to the attached vortex clusters for Case Ma30*Re*15K. The blue and red structures in the middle are the isosurfaces of negative fluctuations of u' and T', respectively. The yellow and green structures at two sides are the isosurfaces of positive fluctuations of u' and T', respectively. The slice at $R_x = 1.5$ shows the contour of the wall-normal velocity. (*b*) The streamwise distributions of the averaged centre height of the positive structures at two sides. Here —— denotes velocity structures and - - - - denotes temperature structures.

streamwise vortex identified by Δ criterion. Given that the vortex clusters exhibit self-similarity (del Á lamo *et al.* 2006), a conditional average is performed within the wall-attached vortex clusters with different scales. The velocity and temperature fluctuation fields surrounding the vortex are rescaled based on the height of the structure's centre. The formula for the streamwise velocity is presented below, and the other variables can be treated in the same way,

$$\langle u' \rangle (\boldsymbol{R}) = \sum_i y_{c,i}^3 \left[u \left(\boldsymbol{R} y_{c,i} + \boldsymbol{x}_{c,i} \right) - \bar{u} \left(r_y + y_{c,i} \right) \right] / \sum_i y_{c,i}^3, \tag{4.6}$$

where $\boldsymbol{x}_{c,i}$ is the position of the circumscribing box centre of the ith structure, $\boldsymbol{r} = \boldsymbol{x} - \boldsymbol{x}_c$ is the position vector respect to the box centre, with its three components r_x, r_y, r_z, $\boldsymbol{R} = \boldsymbol{r}/y_c$ is the rescaled vector and $\langle\,\rangle$ denotes the conditional average. As shown in (4.6), $y_{c,i}^3$ is assigned as the weight for the average operation. Since the length, width and height of the vortex cluster are nearly proportional to the height of the structure's centre, this weighting factor is effectively equivalent to the volume of the circumscribing box enclosing the structure.

Figure 16(*a*) illustrate the velocity and temperature fluctuation fields after conditional average in Case Ma30*Re*15K. Results from other cases are highly similar and therefore not presented here. The negative fluctuation structures in the middle are accompanied by two positive fluctuation structures, as depicted by the isosurfaces for both streamwise velocity and temperature. Similar findings have also been reported by del Á lamo *et al.* (2006) in incompressible flow. Additionally, a slice at $R_x = 1.5$ is provided, revealing that the negative fluctuation structures align with the positive v regions in the spanwise direction, coincidentally meeting the definition of Q2 events. In this region, the streamwise velocity (blue structures) and temperature (red structures) fluctuation structures exhibit strong similarity, indicating that the streamwise vortex transports both velocity and temperature from lower height regions to higher regions via Q2 events. Conversely, in the regions on either side, the positive fluctuation structures align with the negative v

regions, forming Q4 events. Here, the characteristics of the positive fluctuation structures of streamwise velocity (yellow structures) and temperature (green structures) differ significantly. Figure 16(*b*) presents the streamwise distributions of the averaged centre height of the positive structures on both sides. The velocity structures rise rapidly, whereas the temperature structures remain close to the bottom across all cases. Dong *et al.* (2022*b*) computed the conditional averages of the temperature field based on positive and negative shear stress pairs or heat flux pairs in compressible boundary layer and found that the positive T' structures have smaller inclination angles. This observation suggests that the positive temperature structures and Q4 structures of $T''v''$ are located at the bottom of the vortex packets, and the vortex can only transport velocity structures back to the lower region, not temperature structures.

As previously discussed, the streamwise velocity and temperature exhibit a strong correlation in the near-wall region, characterized by a high overlapping rate of the instantaneous structures (in § 4.1). Additionally, the p.d.f.s of structure size for both attached and detached structures of streamwise velocity and temperature are remarkably similar, including large-scale features (in § 3). The generation mechanism of the LSMs of velocity remains an open question. Neither the hairpin vortex packet mechanism (Kim & Adrian 1999) nor the theory of linear modes with the largest transient growth (del Á lamo & Jiménez 2006) can explain the generation of the LSMs of temperature due to the scalar property of temperature and its governing equation (4.2), which conflict with these explanations. Consequently, this paper proposes that the formation process of LSMs of the velocity carries temperature to form these structures together at the same time. However, due to the different mechanisms in the outer layer, temperature on longer follows the transfer of velocity structures. This also elucidates the absence of large-volume sweep events for temperature around vortex clusters, which contrasts with the behaviour of streamwise velocity.

4.3. *Energy transfer*

The energy transfer between flow structures at different scales is investigated to explore the relationship between the streamwise velocity and temperature. Scale decomposition is performed in the real space using a Gaussian filter,

$$\hat{u}_i^{\sigma}(\boldsymbol{x}) = C(\sigma)\int_V u_i'(\boldsymbol{x}')\exp\left(-\frac{2}{\sigma^2}(\boldsymbol{x}-\boldsymbol{x}')^2\right)\mathrm{d}\boldsymbol{x}', \tag{4.7}$$

where σ is the filter scale and $C(\sigma)$ is the normalization coefficient that ensures the integral of the kernel equals one. Here V is the integral domain, defined as a box centred around $\boldsymbol{x}$ with the dimensions of 2σ in each direction. The filter has also been utilized by Lozano-Durán *et al.* (2016) and Motoori & Goto (2021). They further extended the filtering operation by reflecting the filter with the sign of $\hat{u}_2$ inverted when facing the wall to guarantee the boundary condition, which is also adopted in this study. By applying this low-pass filter, the fields corresponding to the specific scale σ can be obtained by

$$u_i^{\sigma}(\boldsymbol{x}) = \hat{u}_i^{\sigma}(\boldsymbol{x}) - \hat{u}_i^{2\sigma}(\boldsymbol{x}). \tag{4.8}$$

Figure 17 illustrates the velocity fluctuation fields for Case Ma30*Re*15K under various scales. The original field without filtering is processed following (4.7) and (4.8) with $\sigma = 0.1$, 0.2 and 0.4, which are normalized by the channel half-height h. Three fields with different scales, which can also be directly identified from the streamwise streaks,

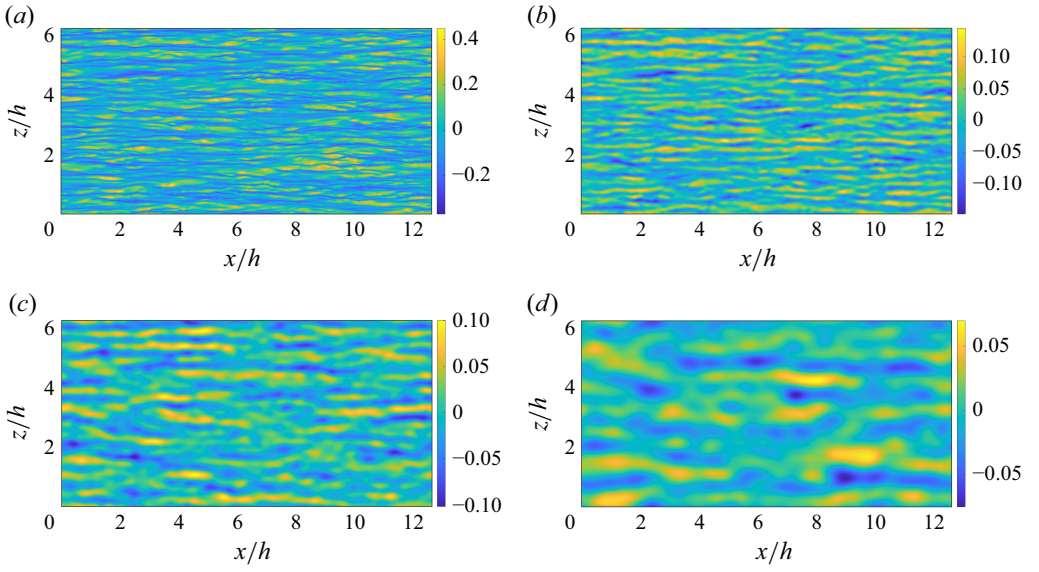

Figure 17. Contour of velocity fluctuation fields at $y^+ \approx 15$ for Case Ma30*Re*15K: (*a*) the original fields without filtering; (*b*) filter scale $\sigma = 0.1$; (*c*) filter scale $\sigma = 0.2$; (*d*) filter scale $\sigma = 0.4$. The scale sizes have been normalized by the channel half-height h.

are obtained. The results demonstrate the successful realization of scale decomposition. Although this decomposition is not strictly orthogonal like Fourier decomposition, the cross-correlation between different scales is sufficiently low, as noted by Motoori & Goto (2021), to support subsequent analysis.

The transport equation of the turbulent kinetic energy $k = u_i'' u_i''/2$ is presented as follows:

$$\begin{aligned}\frac{\partial \bar{\rho}\tilde{k}}{\partial t} + \tilde{u}_j \frac{\partial \bar{\rho}\tilde{k}}{\partial x_j} = &- \bar{\rho}\widetilde{u_i'' u_j''}\frac{\partial \tilde{u}_i}{\partial x_j} - \bar{\rho}\tilde{k}\frac{\partial \tilde{u}_j}{\partial x_j} - \overline{u_j''}\frac{\partial \bar{p}}{\partial x_j} + \overline{p'\frac{\partial u_j''}{\partial x_j}} \\ &- \frac{\partial}{\partial x_j}\left(\overline{p' u_i''}\,\delta_{ij} + \bar{\rho}\widetilde{u_i'' u_i'' u_j''}/2 - \bar{\tau}_{ij}\overline{u_i''} - \overline{\tau_{ij}' u_i''}\right) \\ &- \left(\overline{\bar{\tau}_{ij}\frac{\partial u_j''}{\partial x_j}} + \overline{\tau_{ij}'\frac{\partial u_j''}{\partial x_j}}\right).\end{aligned} \tag{4.9}$$

On the right-hand side of (4.9), The first row contains the production term $-\bar{\rho}\widetilde{u_i'' u_j''}(\partial \tilde{u}_i/\partial x_j)$ and terms related with compressibility. The second and third rows correspond to the diffusion terms and the dissipation terms, respectively. For compressible channel flow, only the wall-normal derivatives in production terms are considered.

To investigate energy production at a specific scale and energy transfer between different scales, fluctuation fields $u_i^{\sigma_1}$ and $u_i^{\sigma_2}$ corresponding to distinct scales σ_1 and σ_2 are extracted from the original flow field, as an example. If more than two scales are considered, the subsequent derivation can be similarly applied. In the similar manner as (4.9) is derived, The transport equation of $k^{\sigma_1} = u_i^{\sigma_1} u_i^{\sigma_1}/2$ can also be derived with the

approximate orthogonality $\overline{\rho u_i^{\sigma_1} u_j^{\sigma_2}} = 0$. The terms concerned in this study are written as

$$Pr_u(\sigma_1, y) = -\bar{\rho}\widetilde{u^{\sigma_1} v^{\sigma_1}} \frac{\partial \tilde{u}}{\partial y}, \tag{4.10}$$

$$Tr_u(\sigma_2 \to \sigma_1; y) = -\overline{\rho u_i^{\sigma_1} u_j^{\sigma_1} \frac{\partial u_i^{\sigma_2}}{\partial x_j}} - \left(\overline{-\rho u_i^{\sigma_2} u_j^{\sigma_2} \frac{\partial u_i^{\sigma_1}}{\partial x_j}} \right). \tag{4.11}$$

The terms above present the energy production of the scale σ_1 and the net energy transfer from the scale σ_2 to the scale σ_1, respectively. The first part on the right-hand side of (4.11) indicates the energy extracted by scale σ_1 from scale σ_2, whereas the direction of the energy transfer for its second part reverses. The other terms are not relevant to the current discussions. The results are also similar to those reported in Motoori & Goto (2021) in incompressible flow.

The turbulent scalar energy $\phi = T''T''/2$ is also defined to investigate the interscale energy transfer of the temperature structures. Its transport equation is also derived here:

$$\begin{aligned}
\frac{\partial \bar{\rho}\tilde{\phi}}{\partial t} + \tilde{u}_j \frac{\partial \bar{\rho}\tilde{\phi}}{\partial x_j} =& -\bar{\rho}\widetilde{T''u_j''} \frac{\partial \tilde{T}}{\partial x_j} - \bar{\rho}\tilde{\phi}\left(1 + \frac{2R_g}{c_v}\right) \frac{\partial \tilde{u}_j}{\partial x_j} \\
&+ \frac{1}{c_v}\overline{T''}\bar{\tau}_{ij} \frac{\partial \tilde{u}_i}{\partial x_j} + \frac{1}{c_v}\overline{\tau_{ij}' T''} \frac{\partial \tilde{u}_i}{\partial x_j} \\
&- \frac{1}{c_v}\overline{\bar{p}T'' \frac{\partial u_j''}{\partial x_j}} - \left(\frac{1}{2} + \frac{R_g}{c_v}\right) \frac{\partial \bar{\rho}\widetilde{T''T''u_j''}}{\partial x_j} \\
&- \frac{1}{c_v}\frac{\partial}{\partial x_j}\left(\bar{q}_j\overline{T''} + \overline{q_j' T''}\right) + \frac{1}{c_v}\left(\bar{q}_j \overline{\frac{\partial T''}{\partial x_j}} + \overline{q_j' \frac{\partial T''}{\partial x_j}}\right) \\
&- \frac{2R_g}{c_v}\overline{\rho u_j'' T'' \frac{\partial T''}{\partial x_j}} + \frac{1}{c_v}\left(\overline{\bar{\tau}_{ij} T'' \frac{\partial u_i''}{\partial x_j}} + \overline{T''\tau_{ij}' \frac{\partial u_i''}{\partial x_j}}\right).
\end{aligned} \tag{4.12}$$

Compared with the turbulent kinetic energy, the turbulent scalar energy has terms related to both velocity and temperature derivatives in its production terms. Similar to the derivation of k^{σ_1}, the energy production and transfer terms for scaler energy ϕ^{σ_1} of scale σ_1 can be written as

$$Pr_T(\sigma_1, y) = -\bar{\rho}\widetilde{T^{\sigma_1} v^{\sigma_1}} \frac{\partial \tilde{T}}{\partial y} + \frac{1}{c_v}\overline{\tau_{12}^{\sigma_1} T^{\sigma_1}} \frac{\partial \tilde{u}}{\partial y}, \tag{4.13}$$

$$Tr_T(\sigma_2 \to \sigma_1; y) = -\overline{\rho T^{\sigma_1} u_j^{\sigma_1} \frac{\partial T^{\sigma_2}}{\partial x_j}} - \left(\overline{-\rho T^{\sigma_2} u_j^{\sigma_2} \frac{\partial T^{\sigma_1}}{\partial x_j}} \right). \tag{4.14}$$

The wall-normal distributions of the production terms of four different cases have been plotted in figure 18. The peak values of all scales in each case are all located within the range of $y^+ = 15$–20 and the structures at this position have been illustrated in figure 17. Mach number effects are evident, as the production terms of the scalar energy are significantly higher when $Ma = 3.0$. For the low Reynolds number cases depicted in figure 18(*a,c*), the production terms of the large-scale velocity structures ($\sigma = 0.4$) at the logarithmic region begin to emerge, despite a monotonic decrease

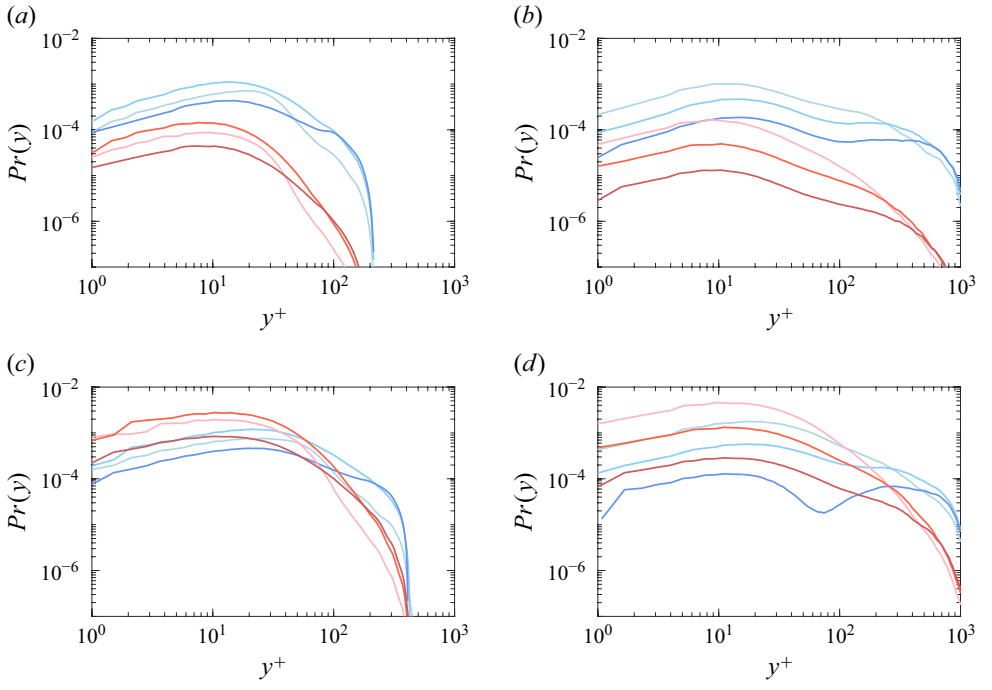

Figure 18. Wall-normal distributions of the production terms of (*a*) Case Ma15*Re*3K, (*b*) Case Ma15*Re*20K, (*c*) Case Ma30*Re*5K and (*d*) Case Ma30*Re*15K. Blue ones denote velocity terms and red ones denote temperature terms. From the lighter one to the darker one denote the scale $\sigma = 0.1$, 0.2 and 0.4, respectively.

beyond the peak position in the near-wall region. However, when compared with the production terms of turbulent kinetic energy, it becomes apparent that the production terms for the large-scale temperature structures are considerably lower and exhibit a rapid decline without undergoing any variation stage. This difference becomes significantly more pronounced for high Reynolds number cases in figure 18(*b,d*). A nearly flat region is observed across almost the entire logarithmic region for the production terms of the large-scale velocity structures, a finding consistent with results from the incompressible flows (Motoori & Goto 2021). In contrast, no similar behaviour is evident for scalar temperature energy. It has been mentioned in § 4.2 that the large-scale negative temperature fluctuation structures are concurrently generated during the formation of velocity structures. However, their behaviours in the outer layer differ markedly. Figure 18 elucidates why temperature structures lack a production mechanism in the outer layer, further indicating that these large-scale temperature structures do not possess the self-sustaining process that is supposed to be featured by the velocity structures (Flores & Jimenez 2006).

The interscale energy transfer $Tr(\sigma_1 \to \sigma_2; y)$ in four cases has been calculated by (4.11) and (4.14) and the results are presented in figure 19. Since the self-energy transfer is zero when $\sigma_1 = \sigma_2$, these lines are omitted from the plots. The blue and red lines denote the energy transfer for velocity and temperature, respectively. From lighter to darker shades of the lines, $\sigma_2 = 0.1$, 0.2 and 0.4. Line types are utilized to differentiate between various values of σ_1 for a given σ_2. For both velocity and

temperature, the interscale energy transfer consistently occurs from the large-scale structures to the small-scale structures, as presented in figure 19. Therefore, large-scale temperature fluctuation structures with large σ, which lack sufficient energy gain from the production terms, experience only energy loss during the interscale energy transfer and dissipate rapidly in the outer layer. As a result, the correlation between the streamwise velocity and temperature is notably low in the outer layer with minimal overlap in their instantaneous distributions. In this study, only structures with an intermediate size ($\sigma = 0.2$) exhibit both energy gain and loss during the transfer process, which will be the primary focus in the subsequent analysis. The position of peak value for the transfer terms in each case, which indicates the height at which interscale interactions are most significant, differs between velocity and temperature structures. For velocity structures with $\sigma = 0.2$, as the Reynolds number increases, they tend to gain energy from larger structures at heights 1.5–2 times their own scale size. The findings for high Reynolds number results are consistent with those reported by Motoori & Goto (2021) in incompressible flow. In contrast, temperature structures do not exhibit such behaviours, and the energy transfer primarily occurs at heights nearly equal to their own scale size. This phenomenon suggests that although the hierarchy of the temperature structures result from the velocity structures, their own mechanism is different from the self-sustaining process of the velocity structures. It should be mentioned that the scale decomposition used here is designed to compare the energy production and interscale energy transfer mechanisms between velocity and temperature. These findings do not correspond directly with those of the structures extracted by the clustering method in § 3. However, it provides a valuable perspective for understanding the decrease in correlation within the outer layer, where large-scale structures dominate. However, with all these phenomena and mechanisms uncovered in this paper, the overall picture of the correlation between velocity and temperature fluctuations in compressible turbulent channel flows from the perspective of coherent structures can be provided, which will be discussed in § 5.

5. Conclusions

The relationships between the streamwise velocity and temperature fields have been investigated in compressible channel flows at different Reynolds and Mach numbers from the perspective of coherent structures. The intense fluctuation structures, the Qs structures and the vortex structures are considered in this study. The identification criteria are summarized in table 2. The threshold values α are decided by the percolation analysis (Appendix), yielding $\alpha = 1.75$, which is consistent with the value adopted by Lozano-Durán *et al.* (2012) and applicable to all five cases considered in this study. To avoid the influences of numerical artefacts, only structures with sizes exceeding $(30/Re_\tau)^3$ are considered in the analysis.

The characteristics of the streamwise velocity and temperature coherent structures are first investigated in § 3. For intense fluctuation structures, the volumes of the negative fluctuation structures u'^- and T'^- dominate, with attached structures being the primary contributors. As the Mach number increases, the volume fractions of all the structures grow. However, the first difference emerges that the positive fluctuation structures of temperature count for only 5 % in Case Ma30*Re*15K, which is significantly lower than the corresponding fraction for velocity. Given that the existence of large-scale structures will enlarge the total volume notably, the extremely low volume fraction indicates a lack

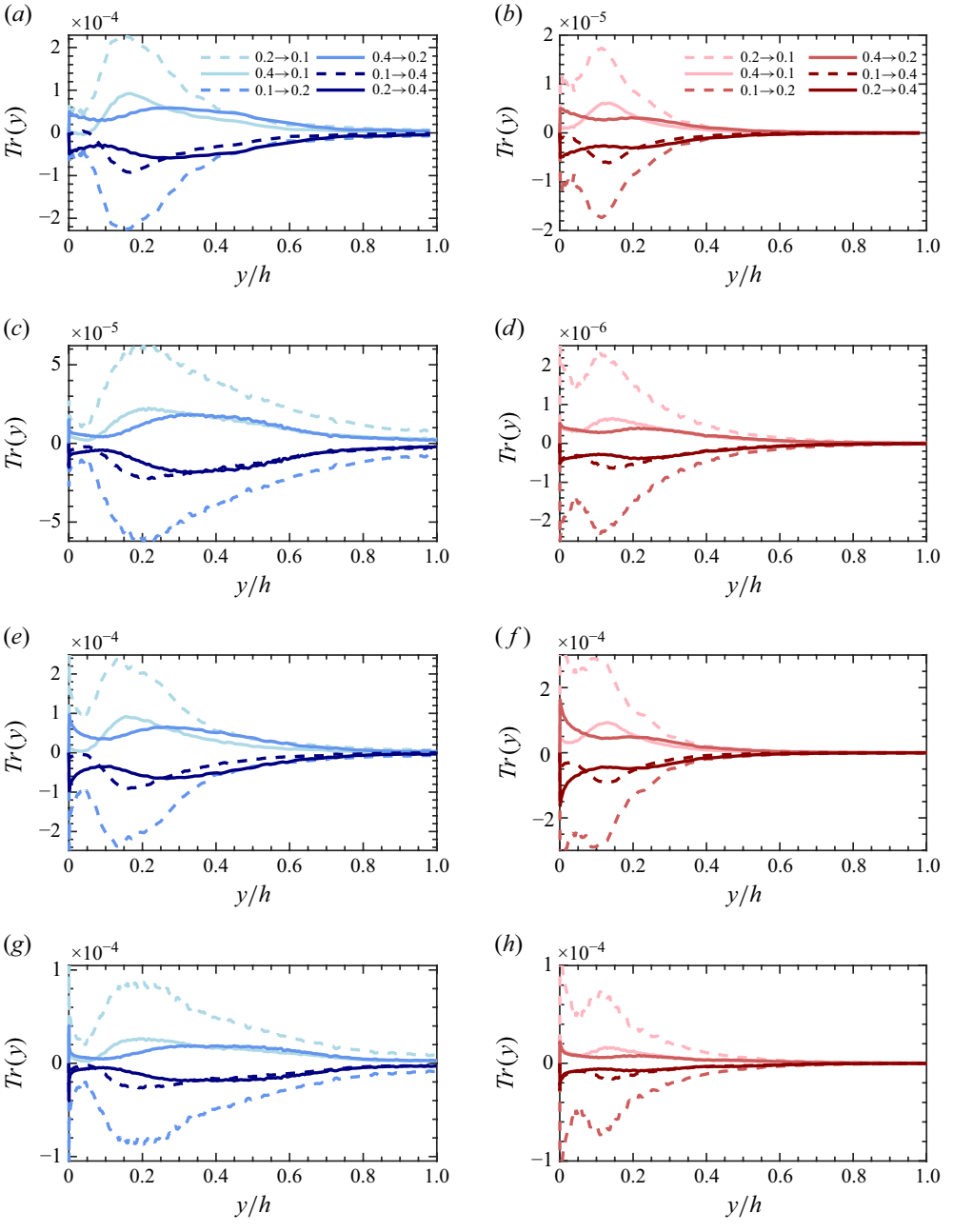

Figure 19. Wall-normal distributions of interscale energy transfer of (*a*,*b*) Case Ma15*Re*3K, (*c*,*d*) Case Ma15*Re*20K, (*e*,*f*) Case Ma30*Re*5K and (*g*,*h*) Case Ma30*Re*15K. The blue lines on the left-hand side belong to velocity and the red lines on the right-hand side belong to temperature. The legend shows the values of $\sigma_1 \rightarrow \sigma_2$ that give the direction of the energy transfer.

of large-scale positive fluctuation structures for temperature in one respect. When the structure size is considered, however, the streamwise velocity and temperature exhibit striking similarities according to the p.d.f.s for both attached and detached structures. The length of the attached intense fluctuation structures exceeds that observed in

incompressible flows. For the attached structures in the outer layer, linear relations $l_x^+ \approx 7.5 l_y^+, l_z^+ \approx l_y^+$ are identified for velocity. In contrast, attached temperature structures are slightly elongated in the spanwise direction, resulting in $l_z^+ \approx 1.1 l_y^+$ instead. This difference, though small, is noteworthy. Furthermore, the increase of Mach number will enhance the elongation effects for both attached velocity and temperature structures. For detached structures in the outer layer, elongation occurs predominantly in the streamwise direction but only for velocity, with the relations obtained being $l_x^+ \approx 1.5 l_y^+$, $l_z^+ \approx l_y^+$. In contrast, the length scales for temperature fluctuations are nearly isotropic across all three directions. Furthermore, the detached fluctuation structures are insensitive to variations in both Reynolds and Mach numbers. Similar observations also apply to Qs structures, where the Q2s (ejection) structures dominate in terms of volume and the Q4s (sweep) structures of temperature are nearly absent with respect to volume contribution. Additionally, the Qs structures of temperature are sensitive to Mach number variations. Compared with intense fluctuation structures, a larger number of flat streaks, whose height is $O(1)$ wall units, are observed. However, the p.d.f.s of the Qs structure sizes show no notable differences. A nonlinear relation $l_x^+ \approx 25(l_y^+)^{0.7}$ is obtained for the Qs structures of both velocity and temperature in the outer layer, with the discrepancy of spanwise length remaining relatively small.

The relationship between streamwise velocity and temperature is further investigated in § 4. The correlation between u' and T' is remarkably strong when $y^+ < 50$, as their governing equations both have diffusion terms with the same form, which play the leading role in the near-wall region. This strong correlation manifests not only in the similarity of structure sizes previously discussed, but also in the high proportion of overlapping pairs observed in the instantaneous field near the wall. Therefore, the high correlation originates from the near-wall region. However, this correlation is diminished by the influence of the outer layer, particularly at high Reynolds number cases where the LSMs and VLSMs play more important roles. The instantaneous distributions of both the intense fluctuation structures and the Qs structures exhibit significant differences, despite the structure sizes remaining similar between streamwise velocity and temperature. This discrepancy arises because the large-scale temperature structures lack the self-sustaining process that is supposed to be held by the velocity structures. This is due to the absence of a production mechanism for large-scale temperature structures in the outer layer, as revealed by budget analysis following scale decomposition. Additionally, the interscale energy transfer mechanisms differ markedly between the velocity and temperature structures. The velocity structures tend to acquire energy at the height twice their own scale size in high Reynolds number cases, whereas the temperature structures do not exhibit such behaviour. For temperature structures, energy transfer predominantly occurs at almost the same height as their own scale size. Therefore, the hierarchy system of the temperature, including the large-scale structures, are not generated by their own dynamic processes. On the contrary, it is the formation process of velocity structures that leads to the generation of temperature structures with similar structure sizes, since the correlation between them is higher in Q2s structures, which transport flow to higher regions. This phenomenon can also be observed in the fields after the conditional average within the attached vortex clusters. In the region of ejection events, the negative fluctuation structures of both velocity and temperature rise up in the downstream. However, upon reaching the outer layer,

the temperature structures are no longer able to align with the velocity structures, leading to completely distinct instantaneous distributions. Furthermore, sweep events fail to bring the temperature structures back to the near-wall region. Conditional average results reveal that the positive fluctuation structures of temperature consistently reside at the bottom of the vortex clusters, while the velocity structures continue to rise up.

In conclusion, the streamwise velocity and temperature exhibit a strong correlation in the near-wall region, characterized by similar structure sizes and a large overlapping rate between their instantaneous structures due to the same form of the diffusion terms in their governing equations. The dynamic process involved in the generation of the hierarchy of velocity structures, such as ejections, enable temperature to follow these structures from the near-wall region until they reach the outer layer, contributing to the remaining correlation in the outer layer. Therefore, the temperature structures also display a hierarchy with similar structure sizes to those of velocity structures, even in the outer layer. However, this passive scalar property cannot provide the production mechanism or the specific interscale energy transfer progress inherent in the hierarchy of the velocity. As a result, the large-scale temperature structures simply decay without undergoing the subsequent dynamic process of velocity, such as the sweeps, leading to significant deviations in their instantaneous distributions from those of velocity structures in the outer layer. The perspective of coherent structures encompasses not only the instantaneous flow structures and their statistical behaviours, but also the momentum and energy transfer processes, as well as many other aspects discussed in this study. It successfully forms a complete picture of the correlation between velocity and temperature fluctuations in compressible turbulent channel flows, which combines phenomena and mechanisms.

Acknowledgements. R.L. would like to thank Z. Zhou at Max Planck Institute for helpful discussions. The authors acknowledge the DNS data provided by Dr C. Cheng from HKUST.

Funding. This work was supported by the National Natural Science Foundation of China (nos. 12422210, 12388101, 92252204). L. Fu also acknowledges the fund from the Research Grants Council (RGC) of the HKSAR Government with RGC/ECS Project (no. 26200222), RGC/GRF Project (no. 16201023), RGC/STG Project (no. STG2/E-605/23-N) and RGC/TRS Project (no. T22-607/24N) and the fund from Guangdong Basic and Applied Basic Research Foundation (no. 2024A1515011798).

Declaration of interests. The authors report no conflict of interest.

Data availability statement. The data within this paper is available upon request.

Appendix

The percolation analysis is performed to determine the threshold α for the identification of coherent structures. In this analysis, the threshold is systematically varied to evaluate the maximum volume fraction of a single structure and the total number of structures. The value of α, which corresponds to both the relatively lower maximum volume fraction and higher number of structures, is selected. The results are presented in figure 20.

It should be mentioned that the exact position of maximum or minimum is not selected, since a trade-off must be achieved between the number of structures and the volume fraction of the largest structure. In this paper, $\alpha = 1.75$ is consistently adopted for all five cases.

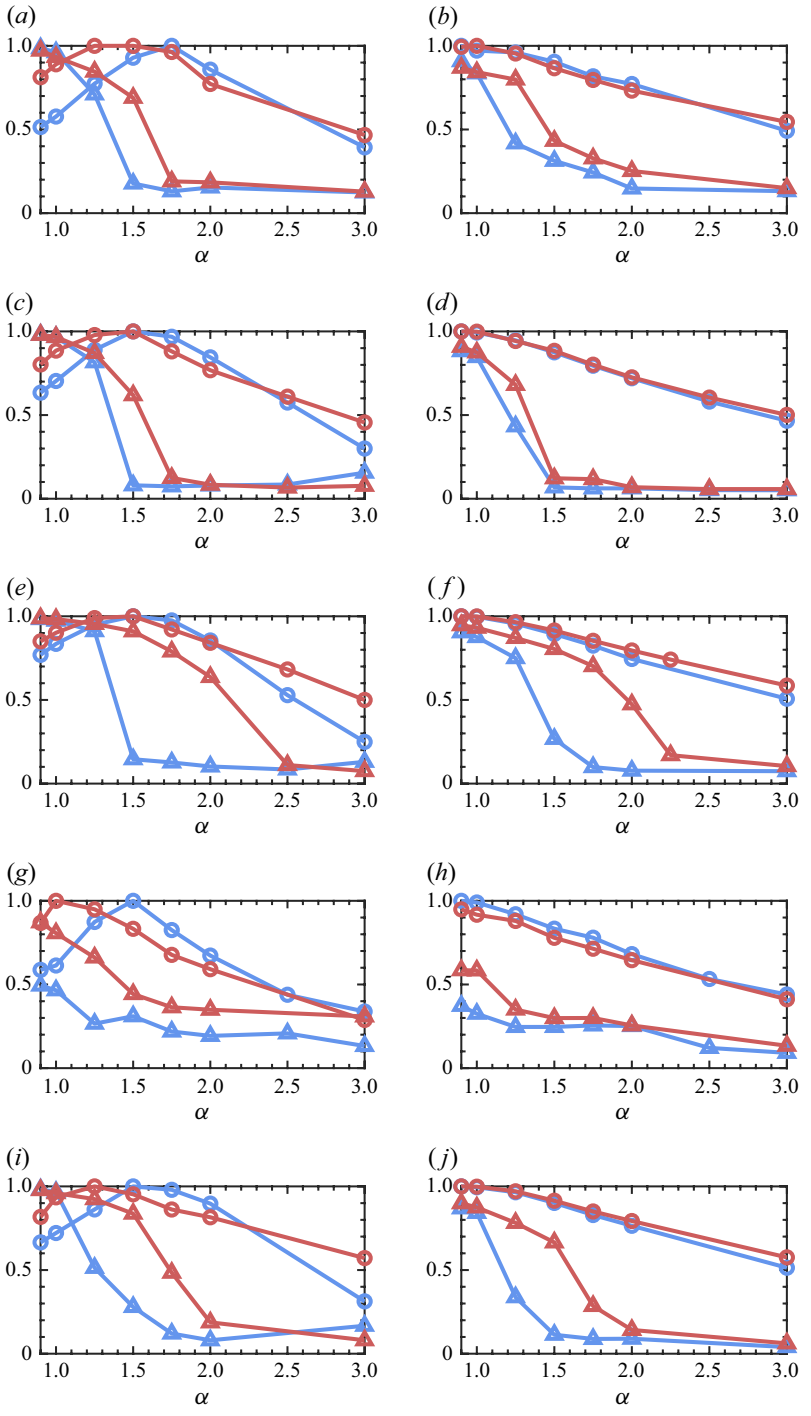

Figure 20. The percolation analysis for α of the following cases: (*a*,*b*) Ma15*Re*3K; (*c*,*d*) Ma15*Re*9K; (*e*,*f*) Ma15*Re*20K; (*g*,*h*) Ma30*Re*5K; (*i*,*j*) Ma30*Re*15K. Blue lines belong to velocity, while red lines stand for temperature. The results for intense fluctuation structures are displayed in (*a*,*c*,*d*,*g*,*i*), whereas (*b*,*d*,*f*,*h*,*j*) contain the results for Qs structures. Lines marked with '○' denote the normalized structure numbers identified using different threshold values of α (normalized by the maximum number), and lines marked with '△' denote the largest single structure volume fraction within the identification results for each α.

References

Adrian, R.J. 2007 Hairpin vortex organization in wall turbulence. *Phys. Fluids* **19** (4), 041301.

Baars, W.J., Hutchins, N. & Marusic, I. 2017 Self-similarity of wall-attached turbulence in boundary layers. *J. Fluid Mech.* **823**, R2.

Bai, T., Cheng, C. & Fu, L. 2024 Investigation of the inclination angles of wall-attached eddies for streamwise velocity and temperature fields in compressible turbulent channel flows. *Phys. Rev. Fluids* **9** (3), 34611.

Bross, M., Scharnowski, S. & Kähler, C.J. 2021 Large-scale coherent structures in compressible turbulent boundary layers. *J. Fluid Mech.* **911**, A2.

Brun, C., Petrovan, B.M., Haberkorn, M. & Comte, P. 2008 Large eddy simulation of compressible channel flow: arguments in favour of universality of compressible turbulent wall bounded flows. *Theor. Comput. Fluid Dyn.* **22**, 189–212.

Chan, C.I. & Chin, R.C. 2022 Decomposition of the reynolds shear stress in a turbulent boundary layer modified by miniature vortex generators. *Phys. Rev. Fluids* **7** (5), 054603.

Chen, X., Cheng, C., Gan, J. & Fu, L. 2023 Study of the linear models in estimating coherent velocity and temperature structures for compressible turbulent channel flows. *J. Fluid Mech.* **973**, A36.

Cheng, C., Chen, X., Zhu, W., Wei, S. & Fu, L. 2024 Progress in physical modeling of compressible wall-bounded turbulent flows. *Acta Mech. Sinica* **40** (1), 323663.

Cheng, Cg & Fu, L. 2022 Large-scale motions and self-similar structures in compressible turbulent channel flows. *Phys. Rev. Fluids* **7** (11), 114604.

Cheng, C. & Fu, L. 2023 Linear-model-based study of the coupling between velocity and temperature fields in compressible turbulent channel flows. *J. Fluid Mech.* **964**, A15.

Cheng, C. & Fu, L. 2024 On the streamwise velocity, temperature and passive scalar fields in compressible turbulent channel flows: a viewpoint from multiphysics couplings. *J. Fluid Mech.* **983**, A38.

Cheng, C., Wei, S. & Fu, L. 2023 Momentum and heat flux events in compressible turbulent channel flows. *Phys. Rev. Fluids* **8** (9), 094602.

Chong, M.S., Perry, A.E. & Cantwell, B.J. 1990 A general classification of three-dimensional flow fields. *Phys. Fluids A: Fluid Dyn.* **2** (5), 765–777.

Cogo, M., Salvadore, F., Picano, F. & Bernardini, M. 2022 Direct numerical simulation of supersonic and hypersonic turbulent boundary layers at moderate–High Reynolds numbers and isothermal wall condition. *J. Fluid Mech.* **945**, A30.

Coleman, G.N., Kim, J. & Moser, R.D. 1995 A numerical study of turbulent supersonic isothermal-wall channel flow. *J. Fluid Mech.* **305**, 159–183.

del Álamo, J. & Jiménez, J. 2006 Linear energy amplification in turbulent channels. *J. Fluid Mech.* **559**, 205.

del Álamo, J., Jiménez, J., Zandonade, P. & Moser, R. 2006 Self-similar vortex clusters in the turbulent logarithmic region. *J. Fluid Mech.* **561**, 329.

Dong, S., Tong, F., Yu, M., Chen, J., Yuan, X. & Wang, Q. 2022*a* Effects of wall temperature on two-point statistics of the fluctuating wall shear stress and heat flux in supersonic turbulent boundary layers. *Phys. Fluids* **34** (6), 65114.

Dong, S., Tong, F., Yu, M., Chen, J., Yuan, X. & Wang, Q. 2022*b* Positive and negative pairs of fluctuating wall shear stress and heat flux in supersonic turbulent boundary layers. *Phys. Fluids* **34** (8), 85115.

Duan, L., Beekman, I. & Martín, M.P. 2010 Direct numerical simulation of hypersonic turbulent boundary layers. Part 2. Effect of wall temperature. *J. Fluid Mech.* **655**, 419–445.

Flores, O. & Jimenez, J. 2006 Effect of wall-boundary disturbances on turbulent channel flows. *J. Fluid Mech.* **566**, 357–376.

Fu, L., Karp, M., Bose, S.T., Moin, P. & Urzay, J. 2021 Shock-induced heating and transition to turbulence in a hypersonic boundary layer. *J. Fluid Mech.* **909**, A8.

Ganapathisubramani, B., Clemens, N.T. & Dolling, D.S. 2006 Large-scale motions in a supersonic turbulent boundary layer. *J. Fluid Mech.* **556**, 271–282.

Ganapathisubramani, B., Hutchins, N., Monty, J.P., Chung, D. & Marusic, I. 2012 Amplitude and frequency modulation in wall turbulence. *J. Fluid Mech.* **712**, 61–91.

Griffin, K.P., Fu, L. & Moin, P. 2021 Velocity transformation for compressible wall-bounded turbulent flows with and without heat transfer. *Proc. Natl Acad. Sci. USA* **118** (34), e2111144118.

Huang, J., Duan, L. & Choudhari, M.M. 2022 Direct numerical simulation of hypersonic turbulent boundary layers: effect of spatial evolution and reynolds number. *J. Fluid Mech.* **937**, A3.

HUANG, P.G., COLEMAN, G.N. & BRADSHAW, P. 1995 Compressible turbulent channel flows: DNS results and modelling. *J. Fluid Mech.* **305**, 185–218.

HUTCHINS, N. & MARUSIC, I. 2007*a* Evidence of very long Meandering features in the logarithmic region of turbulent boundary layers. *J. Fluid Mech.* **579**, 1–28.

HUTCHINS, N. & MARUSIC, I. 2007*b* Large-scale influences in near-wall Turbulence. *Phil. Trans. R. Soc. A: Math., Phys. Engng Sci.* **365** (1852), 647–664.

HWANG, J., LEE, J. & SUNG, H. 2020 Statistical behaviour of self-similar structures in canonical wall turbulence. *J. Fluid Mech.* **905**, A6.

HWANG, J., LEE, J., SUNG, H. & ZAKI, T.A. 2016 Inner–Outer interactions of large-scale structures in turbulent channel flow. *J. Fluid Mech.* **790**, 128–157.

HWANG, J. & SUNG, H. 2018*a* Wall-attached structures of velocity fluctuations in a turbulent boundary layer. *J. Fluid Mech.* **856**, 958–983.

HWANG, J. & SUNG, H.J. 2018*b* Wall-attached structures of velocity fluctuations in a turbulent boundary layer. *J. Fluid Mech.* **856**, 958–983.

JEONG, J., HUSSAIN, F., SCHOPPA, W. & KIM, J. 1997 Coherent structures near the wall in a turbulent channel flow. *J. Fluid Mech.* **332**, 185–214.

KIM, K.C. & ADRIAN, R.J. 1999 Very large-scale motion in the outer layer. *Phys. Fluids* **11** (2), 417–422.

LOZANO-DURÁN, A., FLORES, O. & JIMÉNEZ, J. 2012 The three-dimensional structure of momentum transfer in turbulent channels. *J. Fluid Mech.* **694**, 100–130.

LOZANO-DURÁN, A., HOLZNER, M. & JIMÉNEZ, J. 2016 Multiscale analysis of the topological invariants in the logarithmic region of turbulent channels at a friction reynolds number of 932. *J. Fluid Mech.* **803**, 356–394.

LOZANO-DURÁN, A. & JIMÉNEZ, J. 2014 Time-resolved evolution of coherent structures in turbulent channels: characterization of eddies and cascades. *J. Fluid Mech.* **759**, 432–471.

MAEYAMA, H. & KAWAI, S. 2023 Near-wall numerical coherent structures and turbulence generation in wall-modelled large-eddy simulation. *J. Fluid Mech.* **969**, A29.

MATHIS, R., HUTCHINS, N. & MARUSIC, I. 2009 Large-scale amplitude modulation of the small-scale structures in turbulent boundary layers. *J. Fluid Mech.* **628**, 311–337.

MONTY, J.P., STEWART, J.A., WILLIAMS, R.C. & CHONG, M.S. 2007 Large-scale features in turbulent pipe and channel flows. *J. Fluid Mech.* **589**, 147–156.

MORKOVIN, M.V. 1962 Effects of compressibility on turbulent flows. *Mécanique De LA Turbulence* **367** (380), 26.

MOTOORI, Y. & GOTO, S. 2021 Hierarchy of coherent structures and real-space energy transfer in turbulent channel flow. *J. Fluid Mech.* **911**, A27.

PIROZZOLI, S. & BERNARDINI, M. 2011 Turbulence in supersonic boundary layers at moderate Reynolds number. *J. Fluid Mech.* **688**, 120–168.

REYNOLDS, O. 1961 On the extent and action of the heating surface of steam boilers. *Intl J. Heat Mass Transfer* **3** (2), 163–166.

RINGUETTE, M.J., WU, M. & MARTÍN, M.P. 2008 Coherent structures in direct numerical simulation of turbulent boundary layers at Mach 3. *J. Fluid Mech.* **594**, 59–69.

SMITS, A.J., SPINA, E.F., ALVING, A.E., SMITH, R.W., FERNANDO, E.M. & DONOVAN, J.F. 1989 A comparison of the turbulence structure of subsonic and supersonic boundary layers. *Phys. Fluids A: Fluid Dyn.* **1** (11), 1865–1875.

TOH, S. & ITANO, T. 2005 Interaction between a large-scale structure and near-wall structures in channel flow. *J. Fluid Mech.* **524**, 249–262.

TOWNSEND, A.A.R. 1976 *The Structure of Turbulent Shear Flow*. 2nd edn. Cambridge University Press.

WARK, C.E. & NAGIB, H.M. 1991 Experimental investigation of coherent structures in turbulent boundary layers. *J. Fluid Mech.* **230**, 183–208.

WILLIAMS, O.J., SAHOO, D., BAUMGARTNER, M.L. & SMITS, A.J. 2018 Experiments on the structure and scaling of hypersonic turbulent boundary layers. *J. Fluid Mech.* **834**, 237–270.

XU, D., WANG, J., WAN, M., YU, C., LI, X. & CHEN, S. 2021 Compressibility effect in hypersonic boundary layer with isothermal wall condition. *Phys. Rev. Fluids* **6** (5), 054609.

YAO, J. & HUSSAIN, F. 2020 Turbulence statistics and coherent structures in compressible channel flow. *Phys. Rev. Fluids* **5** (8), 084603.

YUAN, X., TONG, F., LI, W., CHEN, J. & DONG, S. 2022 Wall-attached temperature structures in supersonic turbulent boundary layers. *Phys. Fluids* **34** (11), 115116.

ZHANG, P., WAN, Z., DONG, S., LIU, N., SUN, D. & LU, X. 2023 Conditional analysis on extreme wall shear stress and heat flux events in compressible turbulent boundary layers. *J. Fluid Mech.* **974**, A38.

ZHANG, Y., BI, W., HUSSAIN, F. & SHE, Z. 2013 A generalized reynolds analogy for compressible wall-bounded turbulent flows. *J. Fluid Mech.* **739**, 392–420.

ZHOU, Z., WANG, Y., ZHANG, S., HUANG, W. & XU, C. 2024 Influence of outer large-scale motions on near-wall structures in compressible turbulent channel flows. *J. Fluid Mech.* **994**, A14.

ZHOU, Z., XU, C. & JIMÉNEZ, J. 2022 Interaction between near-wall streaks and large-scale motions in turbulent channel flows. *J. Fluid Mech.* **940**, A23.